



HAL
open science

Constructing dual sulfite-mediated processes via inner-sphere complexation and photogenerated carrier modulation with Hematite/Fe₂TiO₅ heterojunction for ofloxacin degradation

Wenyu Wang, Juntao Guo, Yihui Zhang, Kun Lu, Jing Xu, Jinjun Li, Feng Wu, Gilles Mailhot

► To cite this version:

Wenyu Wang, Juntao Guo, Yihui Zhang, Kun Lu, Jing Xu, et al.. Constructing dual sulfite-mediated processes via inner-sphere complexation and photogenerated carrier modulation with Hematite/Fe₂TiO₅ heterojunction for ofloxacin degradation. *Applied Catalysis B: Environmental*, 2024, 358, pp.124374. 10.1016/j.apcatb.2024.124374 . hal-04646662

HAL Id: hal-04646662

<https://uca.hal.science/hal-04646662>

Submitted on 15 Jul 2024

HAL is a multi-disciplinary open access archive for the deposit and dissemination of scientific research documents, whether they are published or not. The documents may come from teaching and research institutions in France or abroad, or from public or private research centers.

L'archive ouverte pluridisciplinaire **HAL**, est destinée au dépôt et à la diffusion de documents scientifiques de niveau recherche, publiés ou non, émanant des établissements d'enseignement et de recherche français ou étrangers, des laboratoires publics ou privés.



Distributed under a Creative Commons Attribution - NonCommercial - NoDerivatives 4.0 International License

1 **Constructing Dual Sulfite-mediated Processes via Inner-**
2 **sphere Complexation and Photogenerated Carrier**
3 **Modulation with Hematite/Fe₂TiO₅ Heterojunction for**
4 **Ofloxacin Degradation**

5

6 **Wenyu Wang ^a, Juntao Guo ^a, Yihui Zhang ^a, Kun Lu ^a, Jing Xu ^{b,c}, Jinjun Li ^a,**
7 **Feng Wu ^{a*}, Gilles Mailhot ^{d**}**

8

9 ^a *Hubei Key Lab of Biomass Resource Chemistry and Environmental Biotechnology,*
10 *School of Resources and Environmental Science, Wuhan University, Wuhan, 430079, P.*
11 *R. China*

12 ^b *State Key Laboratory of Water Resources and Hydropower Engineering Science,*
13 *Wuhan University, Wuhan 430072, P. R. China*

14 ^c *Hubei Key Laboratory of Water System Science for Sponge City Construction, Wuhan*
15 *University, Wuhan, 430072, P. R. China*

16 ^d *Univ Clermont Auvergne, Inst Chim Clermont Ferrand, CNRS, F-63000 Clermont*
17 *Ferrand, France*

18

19

20 * Corresponding authors

21 * *E-mail addresses:* fengwu@whu.edu.cn (F. Wu), gilles.mailhot@uca.fr (G. Mailhot)

22 **Abstract**

23 Hitherto, various sulfite-based advanced oxidation processes have emerged with
24 particular vantages of low cost and potential for efficient contaminant degradation,
25 which still requires increasing strategies for addressing its drawback. To achieve
26 system-neutral feasibility and overcome the limitations, a metal oxide composite
27 catalyst Hematite/Fe₂TiO₅ integrated with S-scheme heterojunction was constructed for
28 ofloxacin degradation under S(IV)-visible light conditions. Impressively, the as-built
29 system manifested significant promotion on substrate removal (more than four times
30 the original Fe₂TiO₅), which indicated the accelerated inner-sphere interactions
31 between catalyst and S(IV) with beneficial Vis contributed primarily to the degradation,
32 demonstrating the dual sulfite-mediated effective pathway through modulated
33 photogenerated carriers and oxy-sulfur radical chain reactions. Additionally, the
34 interfacial enhancement by the heterojunction structure was further investigated by
35 First-principles computation, which confirmed the mechanism of facilitated electron-
36 hole pair separation. Overall, this work reveals the critical mechanism of Vis-induced
37 S(IV)-AOP and provides constructive perspectives to address the limitations of
38 conventional processes.

39

40 **Keywords:** S(IV)-AOPs, Visible light photocatalysis, Metal oxide composites, First-
41 principles computation, S-scheme heterojunction.

42 1. Introduction

43 Since the quinolone class of antimicrobial agents has gained considerable adoption,
44 its emergence as an emerging contaminant in water bodies has caused detrimental
45 effects on environment, which is unbiodegradable and can lead to the development of
46 antibiotic resistant bacteria [1]. In this aspect, Advanced Oxidation Processes (AOPs)
47 with the productivity of broad-spectrum reactive species have demonstrated
48 outstanding potential in such antibiotic removal techniques, especially sulfate radicals
49 ($\text{SO}_4^{\cdot-}$) based AOPs (SR-AOPs) have attracted extensive attention due to their wider
50 operating pH and more positive potential for substrate oxidation [2, 3]. Nevertheless,
51 the required radicals primarily originate from the persulfate (PS) activation proceedings,
52 which ordinarily accompany the inherent chronic toxicity, secondary pollution by
53 residues, and high cost in progress [4]. Therefore, sulfite (S(IV)) as a typical byproduct
54 from the wet desulfurization process has been utilized for more cost-effective reactive
55 radical production, which has been considered as a prospective substitute for PS in SR-
56 AOPs [5].

57 To date, substantial progress has been made in developing advantageous systems for
58 more effective sulfite-based AOPs (S(IV)-AOPs) [6]. Conventionally, various
59 transition metals (e.g., Fe, Co, Cu, Mn) were proved as the eligible catalysts for the
60 initialization of S(IV) autoxidation whether in homogeneous or heterogeneous system,
61 both the inner-sphere complexation or radical interaction between M^{n+1} and S(IV) can
62 result in the $\cdot\text{SO}_3^-$ production, then $\text{SO}_4^{\cdot-}$ is derived via oxy-sulfur radical chain
63 reactions [7, 8]. Generally, S(IV)-AOPs manifest significant performance at lower pH
64 (2~5) conditions due to the higher proportion of HSO_3^- with less competitive
65 complexation of OH^- , in which heterogeneous process exhibits superiority without the
66 severe drawback of dissolved oxygen (DO) overconsumption at the initial reaction
67 stage [9]. Unfortunately, the relatively low S(IV) & DO utilization efficiencies and
68 surface contamination by sulfite corrosive effect of applied catalyst particles restrict the
69 practical application of heterogeneous S(IV)-AOPs, thus it's of great necessity to seek
70 new strategies and construct novel systems so as to address the limitations [10].

71 As a typical composite transition metal oxide with both surface-active Fe sites and
72 favorable band gap, iron (III) titanium oxide (Fe_2TiO_5) demonstrates prominent
73 potential for the simultaneous activation of S(IV)-based radical reactions and
74 photocatalytic proceedings, which can be effectively exploited to achieve a dual
75 efficiency strategy for the promotion of S(IV)-AOPs through the participation of
76 photogenerated carriers via irradiation [11]. However, although sole Fe_2TiO_5 as an N-
77 type band gap semiconductor shows capability for photocatalytic processes owing to
78 the band edge straddling the water redox potential, its valence band is located in a more
79 positive position and leading to the weaker oxidation capacity of photogenerated holes
80 (h^+) [12]. Additionally, the reactive sites exposed to the catalytic interface are partially
81 occupied by the widespread titanium oxides, resulting in the inhibition of the direct
82 reactivity of Fe_2TiO_5 with S(IV) [13]. Consequently, further catalytic system
83 construction such as heterostructure engineering is demanded to achieve both efficient
84 S(IV) activation and visible light (Vis) responsivity, thus addressing the deficiencies of
85 employed catalyst and making attempts to solve the limitations through Vis irradiation
86 among S(IV)-AOPs. In view of the rational energy band structure alignment and
87 requirement for interaction with S(IV), Hematite with a narrow band gap and suitable
88 valence band edge position is considered a promising candidate for constructing
89 heterojunction with Fe_2TiO_5 [14], attempting to enhance the overall performance
90 through the synergistic effect of S(IV)/Vis processes.

91 Herein, a metal oxide composite catalyst was constructed by Hematite anchoring on
92 Fe_2TiO_5 (Hem/ Fe_2TiO_5) and identified as an S-scheme N-N heterojunction, performing
93 synchronous S(IV) activation and Vis-based photocatalytic process in water treatment.
94 With ofloxacin (OFL, a widely used fluorinated quinolone-type antibiotics) employed
95 as the target contaminant, the performance of the as-constructed Hem/ Fe_2TiO_5 -
96 S(IV)/Vis system under various conditions was evaluated. Through computation and
97 characterization experiments, the enhanced interface effect with internal electric field
98 induced of Hem/ Fe_2TiO_5 was ascertained, thus mechanism for more efficient separation
99 of photogenerated carriers was proposed. Meanwhile, the promotion effect of the Vis-
100 photocatalytic process towards S(IV)-AOPs was observed, thereby the mechanism of

101 dual S(IV)-mediated Processes via inner-sphere complexation and photogenerated
102 carrier modulation was investigated. In addition, the recycling and multi-factor
103 influence experiments were proceeded for feasibility and adaptability verification, and
104 the possible degradation pathway of ofloxacin was also proposed. It can be anticipated
105 that the perspectives to address the limitations of S(IV)-AOPs will expand within the
106 conceive for dual efficiency strategy design.

107

108 **2. Experimental**

109 All chemicals and reagents utilized in this work were commercially available and
110 presented in [Text S1](#). The detailed synthesis of several catalysts was given in [Text S2](#),
111 and the relevant specific experimental operation for degradation was provided in [Text](#)
112 [S3](#) (with [Table S1](#), [Figure S1](#) and [Figure S2](#)). Additionally, different characterization
113 methods for the physicochemical properties of catalysts and analytical methods for
114 degradation proceedings were shown in [Text S4](#) and [Text S5](#) (with [Table S2](#)),
115 respectively. The DFT computational procedures for structural simulation and self-
116 consistency field were presented concretely in [Text S6](#).

117

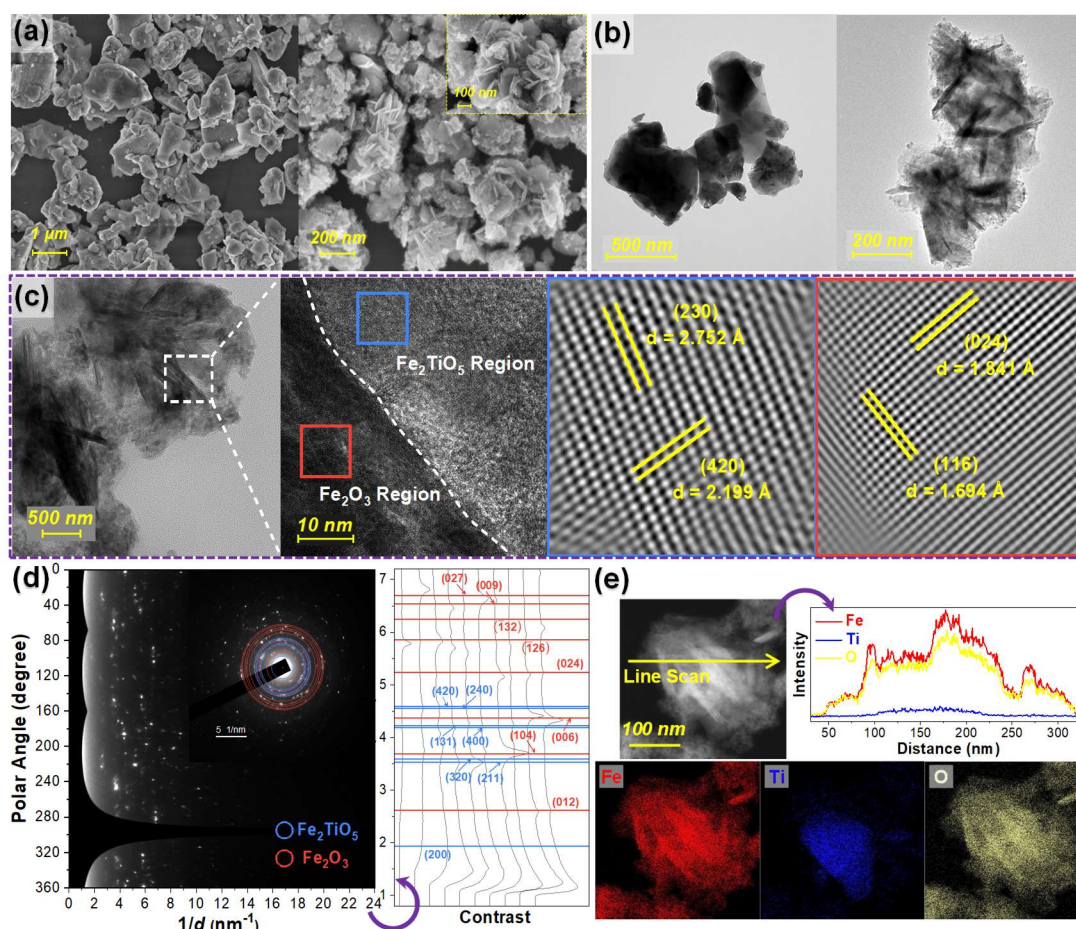
118 **3. Results and discussion**

119 *3.1 Morphological and crystallographic characteristics of catalysts*

120 As a critical part of the synthesis strategy, the modifications in surface morphology
121 and properties of the catalyst with Hematite anchoring were evaluated which primarily
122 determined its behavior in the catalytic reaction. As shown in [Figure 1a](#), raw Fe₂TiO₅
123 (left) possessed a multi-layered block structure and smooth surface with an average
124 diameter of about 1~2 μm, while the block structure remained but with a rougher
125 surface and nearly four times smaller scale in prepared Hem/Fe₂TiO₅ (right). Notably,
126 with the deposition and anchoring composed of immobilized Hematite after
127 hydrothermal and calcination processes, Fe₂TiO₅ could no longer exhibit the uniform
128 distribution of Fe, Ti, and O elements on its surface ([Figure S3](#)), where the Hematite

129 presented in flake accumulations (about 20×100 nm) on its surface causes the
130 significant decrease in Ti proportion (Table S3 and Figure S4). Likewise in the
131 transmission electron microscopy (TEM) images, Hem/Fe₂TiO₅ exhibited a thinner
132 thickness than Fe₂TiO₅ accompanied by most of the Hematite flakes vertically anchored
133 on the surface (Figure 1b). In the high-resolution TEM (HRTEM) images of
134 Hem/Fe₂TiO₅ (Figure 1c), characteristic orthogonal lattice fringes of two distinct
135 regions of difference could be identified (1.694 Å and 1.841 Å, 2.199 Å and 2.752 Å),
136 which were attributed to the (116) and (024) lattice plane of α -Fe₂O₃ [15], (420) and
137 (230) lattice plane of Fe₂TiO₅ [12], respectively. Moreover, the selected area electron
138 diffraction (SAED) patterns with selected integrated intensity curves for representative
139 lattice were visualized and illustrated to further investigate the exposed crystal surface
140 of Hem/Fe₂TiO₅ construction (Figure 1d). Followed by the polar angle regularly
141 unfolded, scattering rings as (200), (211), (320), (400), (131), (240), (420) of Fe₂TiO₅,
142 (012), (104), (006), (024), ($\bar{1}$ 26), ($\bar{1}$ 32), (009), (027) of Fe₂O₃ displayed significantly
143 associated with their crystalline phase own [16]. Whereby indicating the uniform
144 anchoring of Hematite phase with settled crystallographic properties, as well as the
145 properties of internal Fe₂TiO₅ still retained merely along with modifications on the
146 surface. To explore the changes in the elemental distribution before and after
147 preparation in detail, element composition was characterized by the energy dispersive
148 spectrometer (EDS) mapping attached to TEM. As depicted in Figure 1e, denser Fe and
149 O element signals can be observed of Hem/Fe₂TiO₅ which covered both the Fe₂TiO₅
150 precursor and the anchored Hematite, while Fe was slightly higher than O when the line
151 scan swept to Hematite flakes otherwise their ratio was close 1:1. However, Ti in raw
152 Fe₂TiO₅ distributed twice intensities as O and more than ten times as Fe (Figure S5),
153 while it could be perceived inside Hem/Fe₂TiO₅ only. As a result, the characteristic
154 Hematite flakes were dispersed and anchored to Fe₂TiO₅ surface with several exposed
155 crystal planes, which also changed the overall elemental proportion of the catalyst and
156 might contribute to the performance in subsequent degradations.

157



158

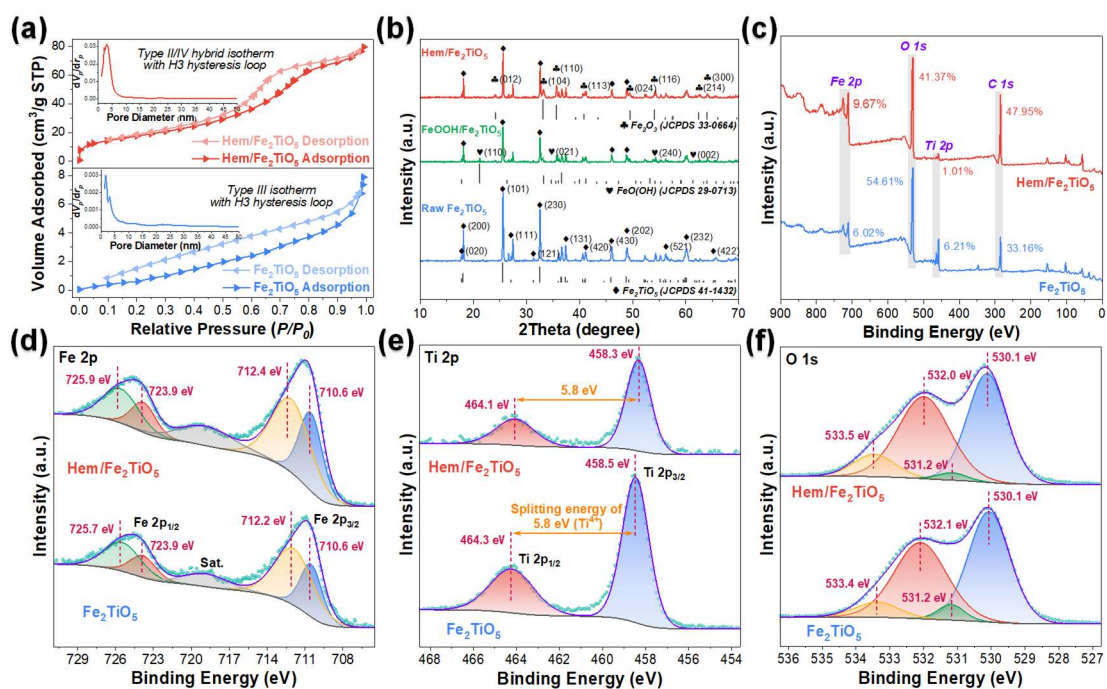
159 **Figure 1** (a) Overall scanning electron microscope (SEM) images of raw Fe₂TiO₅ and synthesized
 160 Hem/Fe₂TiO₅. (b) Localized TEM images of Fe₂TiO₅ and Hem/Fe₂TiO₅. (c) High-resolution TEM
 161 and filtered inverse fast Fourier transform (IFFT) images with lattice fringe markings of
 162 Hem/Fe₂TiO₅. (d) SAED patterns with a polar coordinate expansion of localized Hem/Fe₂TiO₅. (e)
 163 EDS mapping and Line scan images of typical Hem/Fe₂TiO₅ composite region.

164

165 As shown in **Figure 2a**, nitrogen adsorption-desorption measurements were
 166 performed to evaluate the Brunauer-Emmet-Teller (BET) specific surface areas (SSA)
 167 and pore diameter distribution of the as-prepared catalysts. Markedly, two samples
 168 showed characteristic feature curves in their hysteresis loop, which had no limiting
 169 adsorption at high relative pressures and were ascribed to type H3 loops according to
 170 the IUPAC classification, indicating the presence of mesopores in both of them [17].
 171 Besides, Hem/Fe₂TiO₅ (64.747 m²/g) exhibited nearly ten times SSA than Fe₂TiO₅
 172 (6.962 m²/g) with a larger total pore volume (0.123 cm³/g vs. 0.012 cm³/g), which might
 173 due to the staggered distribution of small-scale Hematite flakes on the Fe₂TiO₅ surface.
 174 In practice, this increase in BET-SSA and mesopore distribution can provide abundant

175 reactive sites and facilitate the mass transfer during the heterogeneous reaction process
176 [18]. Furthermore, the phase structures of products at different steps in the preparation
177 of required catalysts were determined via an X-ray diffractometer (XRD). In Figure 2b,
178 the notable diffraction peaks located at 18.1 °, 25.5 °, 32.5 ° presented in all three
179 samples could be indexed to (200), (101), (230) planes of iron (III) titanium oxide
180 (JCPDS 41-1432) [19], which were roughly similar throughout the synthesis procedures
181 and revealed the preservation of the original crystal structure of Fe₂TiO₅. After
182 hydrothermal treatment, it could be observed that several characteristic peaks at 21.2 °,
183 34.7 ° corresponding to the (110), (021) planes of iron oxyhydroxide (FeOOH) (JCPDS
184 29-0713) [20], and eventually disappeared as the calcination proceeded. Notably in the
185 final product of synthesis, prominent crystalline signals at 24.1 °, 33.2 °, 35.6 °
186 corresponding to the (012), (104), (110) planes of α-Fe₂O₃ can be identified with the
187 coexistence of Fe₂TiO₅ [13], illustrating the favorable anchoring of Hematite which was
188 consistent with the SEM and TEM results. Similarly, the changes in elemental state
189 distribution from Fe₂TiO₅ to Hem/Fe₂TiO₅ in X-ray photoelectron spectroscopy (XPS)
190 survey spectrum demonstrated the same results with EDS, and Ti manifested to
191 decrease significantly along with the significant increase in Fe:O ratio (Figure 2c).
192 Interestingly, the splitting energy of Fe 2p deconvolution peaks centered at 712.2 eV
193 and 725.7 eV slightly shifted to a higher energy level by 0.2 eV after Hematite
194 anchoring (Figure 2d), confirming the intruding of Hematite into intercrystallite space
195 of Fe₂TiO₅ and resulting in the variation of Fe chemical state. Furthermore, though the
196 splitting energy of 5.8 eV between two Ti 2p deconvolution peaks indicated the normal
197 oxidation state of Ti⁴⁺ (Figure 2e), the shift of both characteristic peaks represented the
198 emergence of defective Ti³⁺ sites [21]. Deriving from the comparison, the chemical state
199 transformation of O (Figure 2f) followed by the reverse direction shifts of Fe and Ti
200 binding energies signifying the incorporation of Hematite cell into Fe₂TiO₅ matrix, and
201 forming distinct Fe-O-Ti constitution at the interface of two phases [22], which also
202 implied its potential for photocatalytic process with the benefit of electron migration in
203 heterojunction construction [23, 24].

204



205

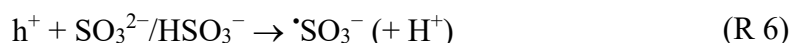
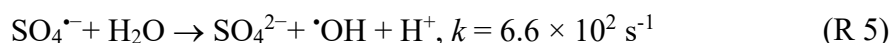
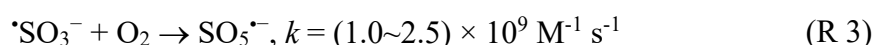
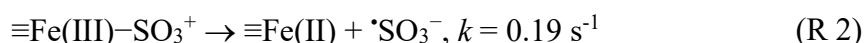
206 **Figure 2** (a) Adsorption-desorption isotherms and pore diameter distributions of Fe₂TiO₅ and
 207 Hem/Fe₂TiO₅. (b) XRD patterns of in-process catalysts during the three-step synthesis procedure.
 208 (c) XPS survey spectrum and atomic proportion of Fe₂TiO₅ and Hem/Fe₂TiO₅. The high-resolution
 209 XPS deconvolution spectra of Fe 2p (d), Ti 2p (e), O 1s (f), respectively.

210

211 3.2 Catalytic degradation performance and system monitoring

212 To investigate the behavior of the catalysts used in S(IV)/Vis integrated system,
 213 degradation experiments were carried out in parallel conditions using ofloxacin (OFL)
 214 as the substrate (Figure 3a). Typically, neither OFL-S(IV), OFL-Vis nor OFL-S(IV)/Vis
 215 could demonstrate significant catalytic removal capacity without catalyst addition,
 216 demonstrating that OFL cannot be degraded directly by reduction of S(IV) or
 217 photosensitization of visible light. Once Fe₂TiO₅ or Hem/Fe₂TiO₅ was utilized in the
 218 system, the present S(IV) was triggered to generate reactive radicals ([•]SO₃⁻) attributed
 219 to the inner-sphere interaction between ≡Fe(III) and SO₃²⁻/HSO₃⁻ (Reaction 1 and 2),
 220 subsequently more oxidizing active species (SO₅^{•-}, SO₄^{•-} and [•]OH) were produced
 221 through oxy-sulfur radical chain reactions (Reaction 3~5) [25]. In the meantime, the
 222 substrate OFL was removed along with the production of such radicals, yet the
 223 degradation was restricted in both OFL-Catalyst-S(IV) systems and mainly in the early
 224 part of the reaction (before 20 min). Herein, OFL-Catalyst-S(IV)/Vis systems were
 225 examined which revealed the significant promotion by visible light irradiation with

226 Hem/Fe₂TiO₅, which might be attributed to the synergistic effect among sulfite-AOP
 227 with photocatalysis process mediated by the as-prepared Hem/Fe₂TiO₅. Generally, the
 228 photogenerated holes (h⁺) were thought to attack the substrate directly, but a more
 229 efficient reaction pathway could be achieved in S(IV) system through the interaction
 230 between h⁺ and S(IV) (Reaction 6), which could address the limitations by dissolved
 231 oxygen (DO) and ≡Fe(III) in S(IV)-AOPs (Reaction 3 and 7) [26].



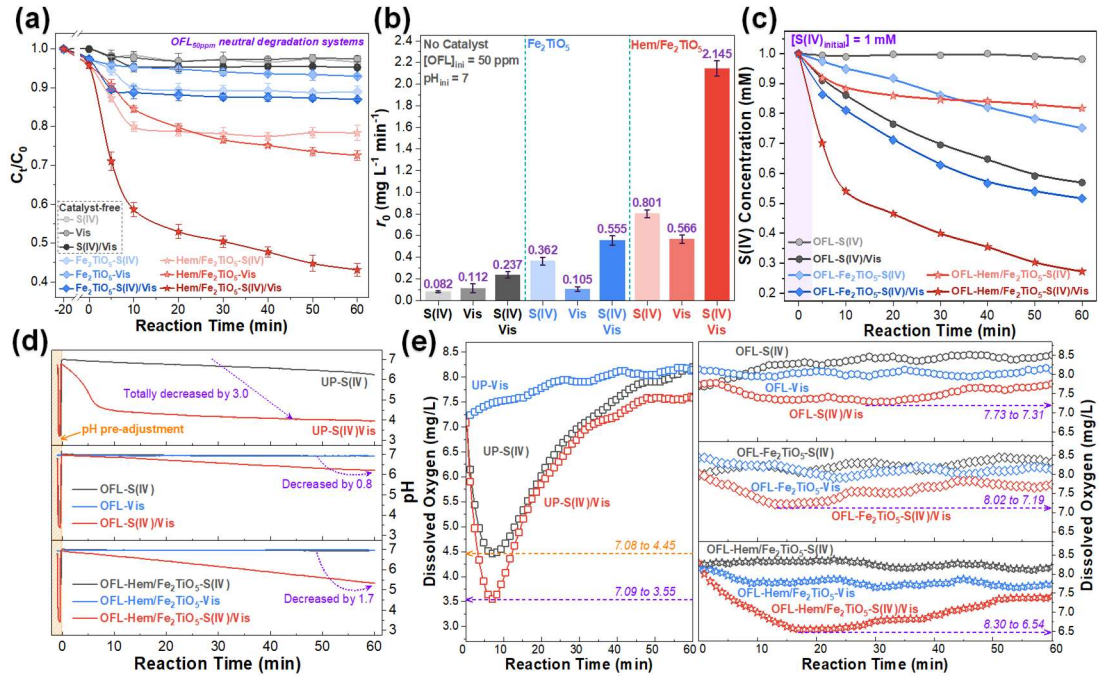
232 Additionally, the designed Hem/Fe₂TiO₅ catalyst manifested better responsiveness
 233 with both S(IV) and Vis compared with the Fe₂TiO₅ precursor, which could exhibit
 234 nearly 4 times increase in initial reaction rates (*r*₀) with S(IV)/Vis process (Figure 3b).
 235 To further understand the reasons for the superiorities of the constructed catalytic
 236 system, the changes in S(IV) concentration of reaction course were monitored (DTNB
 237 method, Text S7 and Figure S6). As shown in Figure 3c, the applied 1 mM S(IV) was
 238 not consumed significantly under neutral conditions without catalysts, even with Vis
 239 available the observed decrease in S(IV) concentration was also entirely attributed to
 240 its accelerated autooxidation and led to little degradation of OFL [27]. For comparison,
 241 S(IV) was obviously consumed in the presence of Fe₂TiO₅ or Hem/Fe₂TiO₅, where the
 242 latter could achieve more OFL degradation with less S(IV) consuming conditions.
 243 What's more, this regularity was even more pronounced when applying the S(IV)/Vis
 244 dual conditions, indicating the more efficient utilization mediated by Hem/Fe₂TiO₅.
 245 Given that the Hematite anchoring undertaken principally contributed to their
 246 difference in performance, Hematite prepared individually and its standard industrial
 247 product from MACKLIN were employed for separate control experiments. Specifically,

248 the as-prepared Hematite showed essentially the same characteristic signals of XRD
249 patterns with the industrial product (Figure S7) and could exhibit greater reactivity with
250 S(IV) but Vis inversely (Figure S8a). Experiments on the physical co-mixing as per the
251 synthetic ratio also demonstrated that the designed and synthesized heterojunction by
252 Hematite with Fe₂TiO₅ played a decisive role on the oxidative degradation of substrates,
253 while the industrial products always fell short (Figure S8b). Moreover, the leaching
254 Fe_{total} remained in each of the above system was determined by atomic absorption
255 spectroscopy (AAS) with the standard curve provided in Figure S9a. It can be observed
256 the surface stabilization of Hematite_{industrial}, Fe₂TiO₅ and synthesized Hem/Fe₂TiO₅ in
257 UP for a long period, but Hematite_{synthesized} manifested excessive leaching (566.4 μg/L)
258 after 60 min which was twenty times more than 0 min. Likewise after the S(IV)/Vis
259 process, the leaching amount with Hematite_{synthesized} was still the most pronounced
260 while Hematite_{industrial} and Fe₂TiO₅ exhibited slighter, Hem/Fe₂TiO₅ remained stable
261 with practically unchanged Fe_{total} concentration (Figure S9b), demonstrating that
262 synthesized Hematite with greater reactivity only when anchored can reduce the
263 leaching while retain its performance.

264 In recognition that the variance in pH and DO are especially critical for S(IV)-AOPs,
265 the periodic changes of both were also continuously monitored during typical
266 degradation systems. As illustrated in Figures 3d and 3e, neither the OFL-S(IV) nor the
267 OFL-Vis systems under neutral could have a significant effect on pH and DO, whereas
268 it can be found the rapid pH reduction trend and DO depletion-supplementation
269 proceeding with OFL being replaced by UP [28]. Obviously, it was proved that visible
270 light did promote the interaction of S(IV) series reactions with molecular oxygen, but
271 the reasons under the absence or presence of catalysts were divided into the facilitated
272 autooxidation or autoxidation of S(IV), respectively [6]. And due to the buffering effect
273 initiated by different dissociation states of OFL, the pH of several systems was less
274 likely to decrease with the DO consumption also being inhibited, then deactivating the
275 oxy-sulfur radical chain reactions [29]. Notably, Fe₂TiO₅ and Hem/Fe₂TiO₅ dosing
276 under neutral OFL conditions could reactivate the regular S(IV) autoxidation to varying
277 degrees, simultaneously decelerate the overly rapid pH and DO changing processes

278 compared to the homogeneous reaction, which can certainly reduce the proportion of
 279 invalid S(IV) autooxidation in the degradation process with improved energy efficiency
 280 and removal performance [30].

281



282

283 **Figure 3** (a) Degradation of OFL in various catalyst-S(IV)/Vis systems. (b) Corresponding initial
 284 reaction rates within different systems. (c) Changes of S(IV) concentration under different catalytic
 285 conditions. Continuous monitoring curves for pH (d) and DO (e) in various control experiments.
 286 Conditions: [OFL] = 50 ppm, [Catalyst] = 0.5 g/L, [S(IV)] = 1 mM, pH = 7, under Vis-irradiation.

287

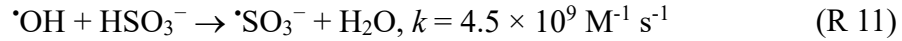
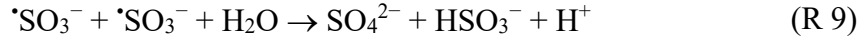
288 3.3 Variances in removal efficiency with different influencing factors

289 In order to further investigate the performance of the advantageous Hem/Fe₂TiO₅-
 290 S(IV)/Vis process under different conditions, various gradient experiments were
 291 performed with varying catalyst dosages, initial OFL concentrations, initial pH settings,
 292 and initial S(IV) concentrations, respectively. As depicted in Figure 4a, the OFL
 293 degradation was obviously enhanced with the Hem/Fe₂TiO₅ dosage increase from 0.1
 294 g/L to 0.5 g/L, as well as r_0 became markedly more rapid. However, although the r_0
 295 enhancement due to the increased catalyst dosing was still evident, the facilitating effect
 296 began to mitigate when the dosage exceeded 0.75 g/L. Eventually, as the final
 297 degradation rates converged, it can be hypothesized that excessive catalyst addition in
 298 solution led to less effective irradiation absorption, and thus cannot always benefit the

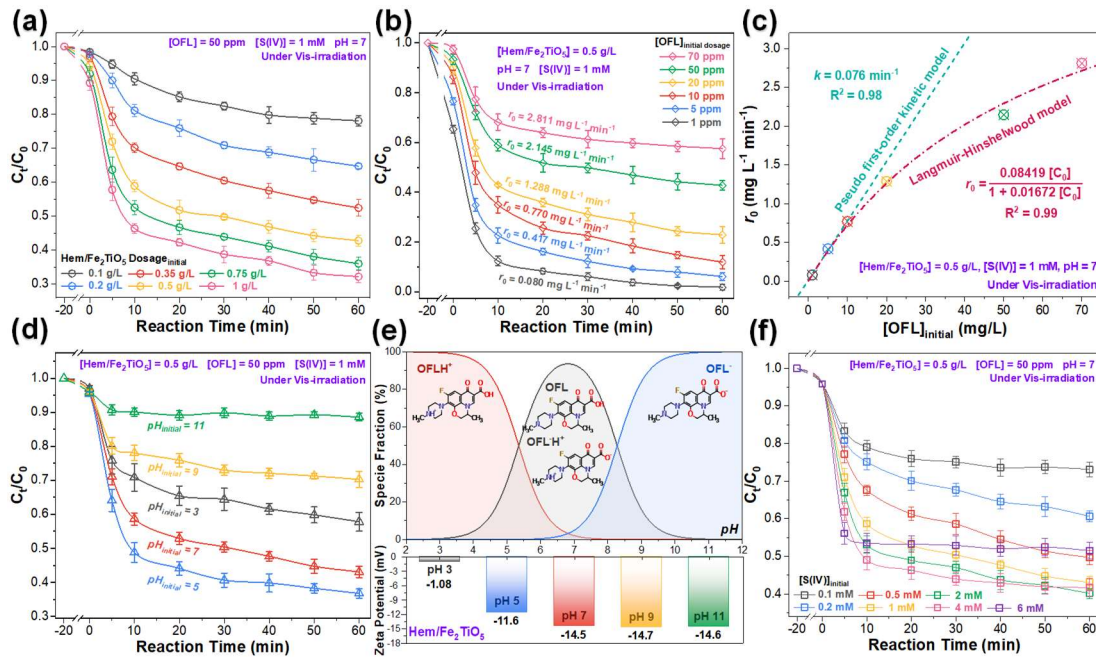
299 degradation system [31]. The kinetic behavior of the Hem/Fe₂TiO₅-S(IV)/Vis system
300 was also explored by varying the initial concentration of substrate OFL (Figure 4b). It
301 can be observed that the degradation reaction at different OFL concentrations proceeded
302 the fastest within the first 10 min and became remarkable with the decrease of OFL,
303 indicating the rate limitation by both heterogeneous interaction and mass transfer in
304 solution during the reaction course. By fitting the kinetic models to the different
305 degradation stages, the pseudo-first order kinetic constant ($k = 0.076 \text{ min}^{-1}$) was
306 obtained in the initial 10 min, while the overall degradation process within 60 min was
307 consistent with the Langmuir-Hinshelwood kinetic model as well (Text S8 and Figure
308 4c) [32].

309 Given the significant influence of initial pH on the reaction efficiency of S(IV)-AOPs,
310 separate control experiments in specific pH conditions were performed. As predicted,
311 the OFL degradation capacity of the Hem/Fe₂TiO₅-S(IV)/Vis system phased down
312 under alkaline conditions ($\text{pH} > 7$), even only minimal OFL removal was obtained at
313 $\text{pH} = 11$ within the very beginning reaction stage (Figure 4d), which has been attributed
314 to the competitive binding of hydroxyl groups and S(IV) to reactive $\equiv\text{Fe(III)}$ sites [33].
315 Despite the OFL degradation being promoted when the initial pH was lowered to 5,
316 closely then it rebounded to be inhibited with the pH continually decreasing to 3.
317 Considering OFL as an organic compound has multiple dissociated forms [29], the
318 chemisorption affinity between the catalyst surface and OFL substrate at different pH
319 was evaluated by zeta potential (ζ). As shown in Figure 4e, the surface of Hem/Fe₂TiO₅
320 is negatively charged at different pH, but raised to near the isoelectric point with pH
321 decreased to 3. Therefore, the chemisorption between OFL⁺ and Hem/Fe₂TiO₅ was
322 weakened as the system tends to become more acidic, contributing to the inhibited
323 degradation of OFL at $\text{pH} = 3$ [34]. Additionally, the effects of different initial S(IV)
324 concentrations on OFL degradation were revealed in Figure 4f. Notably, the OFL
325 degradation rate increased significantly with increasing S(IV) until its concentration
326 reached 2 mM, then deceleration of the reaction process occurred at 4 mM S(IV) and
327 eventually the subsequent reaction was almost completely inhibited at the highest
328 concentration as 6 mM S(IV). In practice, this retardation effect at higher S(IV)

329 concentration or the leveling off phenomenon could be rationalized by the self-
 330 scavenging effect of $\cdot\text{SO}_3^-$ due to overdosed sulfite (Reaction 8 and 9), and/or the
 331 competition of sulfite with other generated active species (Reaction 10 and 11) [11].



332



333

334 **Figure 4** (a) Differences in OFL degradation efficiencies at different initial Hem/Fe₂TiO₅ dosages.
 335 Various degradation efficiencies at different initial OFL concentrations (b) along with corresponding
 336 pseudo-first order kinetic equation fitting and Langmuir-Hinshelwood kinetic modeling (c). (d)
 337 Performance in OFL degradation of Hem/Fe₂TiO₅-S(IV)/Vis system at different initial pHs. (e)
 338 Dissociated state distribution of substrate OFL and surface ζ potential distribution of Hem/Fe₂TiO₅
 339 at different pH. (f) Degradation behavior differences of catalytic system with diverse initial S(IV)
 340 concentrations.

341

342 3.4 Evaluation of apparent photoelectrochemical properties

343 Photoelectrochemical characterizations of Hem/Fe₂TiO₅ and its precursor Fe₂TiO₅
 344 were carried out for deeper understanding and evaluation of their behavioral differences
 345 on degradation performance, as well as the vigorous contribution of the anchored
 346 Hematite to the overall catalyst, preparation of optical electrodes and electrochemical

347 parameters were provided in [Text S9](#). The intermittent photocurrent responsive curves
348 were demonstrated in [Figure 5a](#), where Fe_2TiO_5 only exhibited a weak charge transfer
349 capacity but nearly twice the previous current density after anchoring Hematite can be
350 observed. In carrying out the irradiation on/off cycles with an interval of 30 s,
351 Hem/ Fe_2TiO_5 showed a current density difference of about 3.8 times that of Fe_2TiO_5 ,
352 indicating its enhanced photogenerated carrier separateness [\[35\]](#). Moreover, the charge
353 transfer and recombination processes were also investigated by electrochemical
354 impedance spectroscopy (EIS) as shown in [Figure 5b](#). After their equivalent circuit
355 simulations by Nyquist plots, the ohmic impedance (R_s) of Hem/ Fe_2TiO_5 and Fe_2TiO_5
356 was approximate while constant-phase angle element CPE-T (double-layer capacitance,
357 Cdl) existed within the same order of magnitude, which means the similar
358 electrochemically active area of them [\[36\]](#). However, the electrode-electrolyte charge
359 transfer resistance (R_{ct}) and Warburg impedance (W_0 -R) of Hem/ Fe_2TiO_5 clearly
360 decreased, demonstrating the anchoring with Hematite did increase the charge transfer
361 rate across the heterogeneous interface, which also reduced the recombination of
362 photogenerated carriers and thus enhance the resulting photocurrent [\[37, 38\]](#).

363 After verifying the differences in photoreactivity between Fe_2TiO_5 and Hem/ Fe_2TiO_5 ,
364 the energy band alignments were characterized and calculated to clarify the interfacial
365 recombination process of as-constructed heterojunction. With the two catalysts and bare
366 Hematite were tested by UV/Vis diffuse reflectance spectroscopy (UV/Vis-DRS)
367 ([Figure 5c](#)), it can be obtained that Hem/ Fe_2TiO_5 exhibited similar absorption intensity
368 at long wavelength region to that of bare Hematite, which was due to the blockage of
369 the d-orbital transition in the direct photon excitation of Fe_2TiO_5 by anchored Hematite.
370 However, Hem/ Fe_2TiO_5 with the presence of N-N heterojunction demonstrated stronger
371 absorption in the sub-650 nm band, with its band gap (BG) decreased by 0.14 eV
372 compared with Fe_2TiO_5 (1.97 eV) and becomes more inclined to be excited by Vis
373 directly [\[39\]](#).

374 In the Mott-Schottky electrochemical analysis depicted in [Figure 5d](#), both catalysts
375 manifested N-type semiconductor properties at different frequencies with their
376 corresponding flat band potentials (E_{FB}) calculated by the average of linear

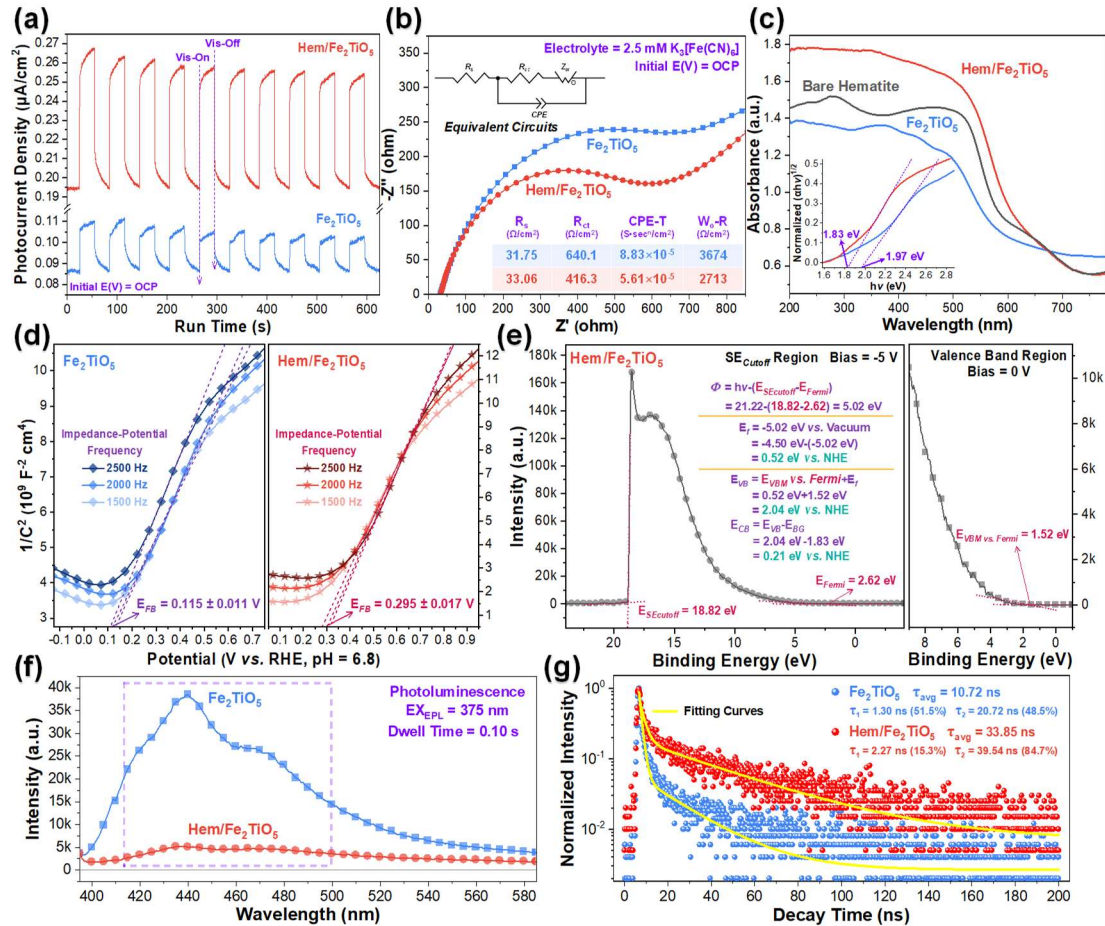
377 extrapolations. Afterwards, the energy band alignment of Hem/Fe₂TiO₅ was further
 378 verified by UV photoelectron spectroscopy (UPS) applying -5 V and 0 V bias,
 379 respectively. The work function was calculated as the energetic difference between the
 380 Fermi and Vacuum levels as defined by the secondary-electron cutoff edge, and the
 381 ionization energy was estimated as the onset of the density of states at valence band
 382 maximum [40]. As illustrated in Figure 5e and the inset equations, the work function
 383 (Φ) of 5.02 eV and the Fermi energy level (E_f) at 0.52 eV vs. NHE can be obtained.
 384 Likewise, the valence band (E_{VB}) and conduction band (E_{CB}) of Hem/Fe₂TiO₅ were
 385 calculated to be situated at 2.04 eV vs. NHE and 0.21 eV vs. NHE, respectively, which
 386 were in fairer correspondence with the results in UV/Vis-DRS and Mott-Schottky
 387 analysis.

388 Additionally, the steady-state photoluminescence spectra (PL) and time resolved
 389 photoluminescence spectra (TRPL) were utilized to probe the effect of heterojunction
 390 formation on the photoexcitation process and carrier production. As depicted in Figure
 391 5f, raw Fe₂TiO₅ gave a large emission band in visible light region around 410~500 nm
 392 while excited by 375 nm laser. As for the Hem/Fe₂TiO₅ integrated with N-N
 393 heterojunction, though similar emission signal range can be observed, its characteristic
 394 intensity greatly weakened. This unambiguously reflects the recombination of the
 395 electron-hole pairs was much inhibited with the construction of heterojunction compare
 396 to the individual phase as in Fe₂TiO₅ [41]. Then the separation and recombination of
 397 photogenerated carriers were further evaluated through TRPL spectroscopy with a 375
 398 nm pulsed laser, while the results were fitted by the biexponential decay function to
 399 obtain partial (τ_1 , τ_2) and average lifetimes (τ_{avg}) of different carriers (Eq 1).

$$R(t) = B_1 e^{-t/\tau_1} + B_2 e^{-t/\tau_2} \quad (\text{Eq 1})$$

400 As shown in Figure 5g, the calculated radiation lifetimes of Fe₂TiO₅ ($\tau_{avg} = 10.72$ ns)
 401 were mainly divided into short-lived ($\tau_1 = 1.30$ ns, $B_1 = 51.5\%$) and long-lived ($\tau_2 =$
 402 20.72 ns, $B_2 = 48.5\%$) species with a similar proportion, while a significant increase in
 403 the lifetime of both species can be observed ($\tau_1 = 2.27$ ns, $B_1 = 15.3\%$; $\tau_2 = 39.54$ ns,
 404 $B_2 = 84.7\%$) due to the heterojunction behavior of Hem/Fe₂TiO₅. Moreover, the

405 obtained long-lived species in Hem/Fe₂TiO₅ performed more dominant, which
 406 confirmed the realization of longer carrier separation through Hematite anchoring for
 407 the passivation of the surface recombination sites within the S-scheme proceedings [42].
 408



409
 410 **Figure 5** (a) Difference in photocurrent densities between Hem/Fe₂TiO₅ and Fe₂TiO₅ under
 411 intermittent Vis irradiation. (b) EIS-Nyquist impedance plot with equivalent circuit simulation for
 412 both catalysts under identical conditions. (c) UV/Vis DRS spectra of bare Hematite, Fe₂TiO₅ and
 413 Hem/Fe₂TiO₅ with corresponding band gap calculation. (d) Mott-Schottky curves with
 414 corresponding flat band potential obtained by linear extrapolation in specific frequencies. (e)
 415 Biased/unbiased UPS characterizations and energy band alignment calculation of Hem/Fe₂TiO₅. (f)
 416 Photoluminescence spectra of both catalysts at the excitation wavelength of 375 nm. (g)
 417 Decay curves of TRPL with fitted carrier lifetime distribution irradiated by laser pulses probed at 375 nm.

418

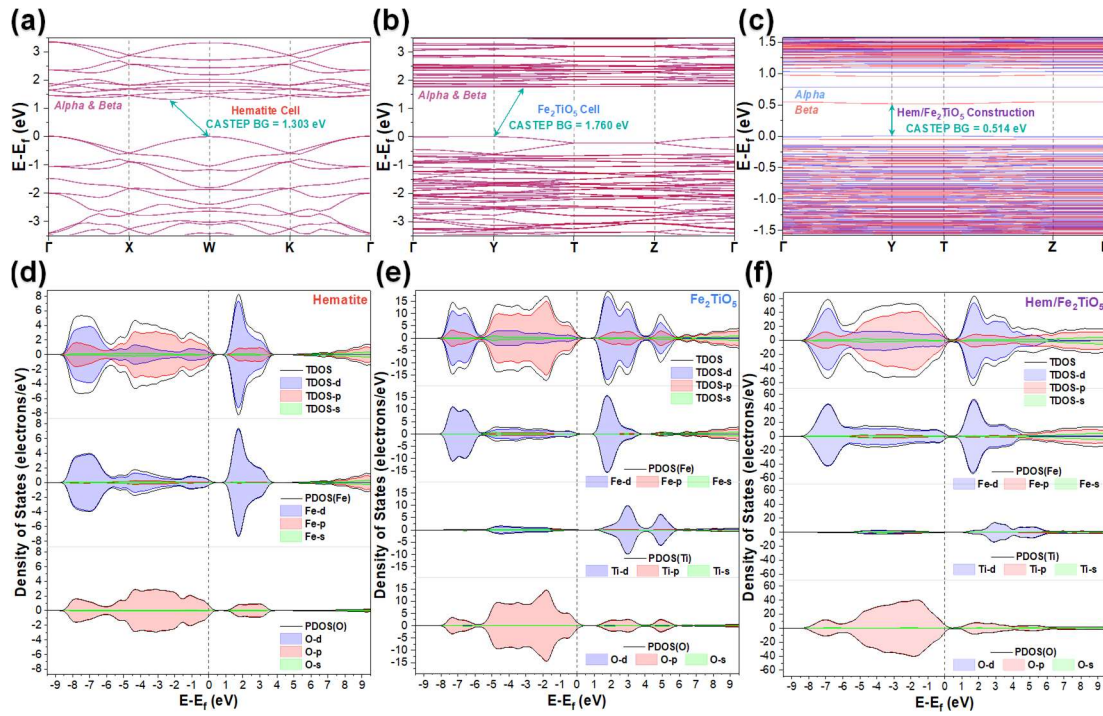
419 3.5 Theoretical model construction and computation

420 In recognition that approximate density functional theory (DFT) has faced challenges
 421 in accurately describing the electronic structure and magnetic properties of iron oxides
 422 due to the confined nature of Fe-3d orbital and the strong self-interaction error (SIE) of

423 Local Density Approximation (LDA) or Generalized Gradient Approximation (GGA)
424 exchange-correlation functionals, hence, the systematic SIE in computational electronic
425 structure and magnetic description of both Hematite and Fe_2TiO_5 needs to be corrected
426 during the geometry optimization and energy minimization processes. For various
427 transition-metal systems, the Hubbard U method (DFT+U) has been considered as a
428 common choice with enhanced accuracy and low computational cost, in which an
429 additional Coulomb repulsion term is added to the approximate DFT energy and the
430 highly localized d or f electrons is described by Hubbard model [43]. Precisely, the on-
431 site DFT+U corrections for the Fe-3d states in the as-constructed Hematite
432 (antiferromagnetic, $U = 4.06$ eV) and Fe_2TiO_5 (ferromagnetic, $U = 3.88$ eV) cells were
433 proceeded with defining the atomic magnetization in initial guess [44, 45], with the
434 cleaved (024) plane of Hematite and (101) plane of Fe_2TiO_5 were selected for the
435 Hem/ Fe_2TiO_5 construction simulation due to HRTEM and XRD indications (Figure
436 S10a~10c). As demonstrated in Figures 6a and 6b, Hematite and Fe_2TiO_5 exhibited
437 indirect band gap and direct band gap properties with BG calculated as 1.303 eV and
438 1.760 eV, respectively. For Hem/ Fe_2TiO_5 composite construction, its valence band
439 maximum (VBM) and conduction band minimum (CBM) were simultaneously located
440 at the same high symmetry point in the Brillouin zone with further reduced BG value
441 (0.514 eV) (Figure 6c), indicating the continuous distribution of energy levels near
442 Fermi level which is conducive to the charge transfer and reactivity. Additionally, the
443 computed partial density of state (PDOS) of Hematite indicated that its VBM were
444 mainly contributed from the p orbital of O and d orbital of Fe, and CBM mainly
445 contributed from the d orbital of Fe and p orbital of O (Figure 6d), which exhibited
446 similarity to Fe_2TiO_5 except for the extra contribution in d orbital from Ti (Figure 6e).
447 Although the addition of Hematite showed less significant effects on the p orbital, the
448 electron distribution in the d orbital varied obviously in Hem/ Fe_2TiO_5 construction.
449 Specifically, a simultaneous increase in the contribution of Fe d orbital to VBM and
450 CBM can be observed with the contribution of Ti d orbital decreased, which led to the
451 orbital overlap and configuration mixing due to the collapse of d orbitals in
452 Hem/ Fe_2TiO_5 (Figure 6f), thereby the emerging electron orbital alignments facilitated

453 the electron transition in heterojunction with lower BG [46].

454



455

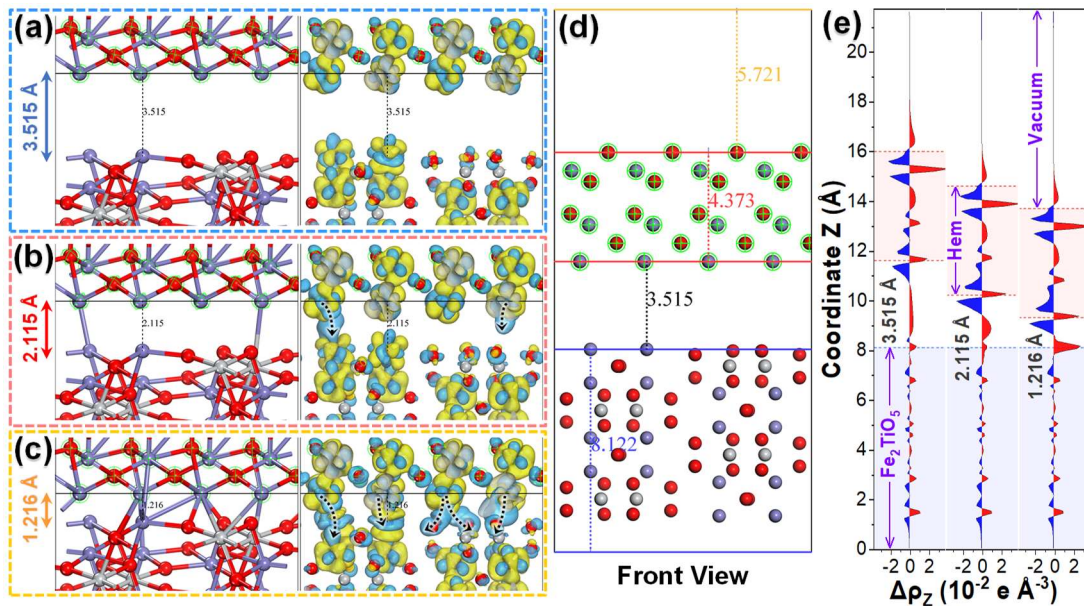
456 **Figure 6** The theoretical band structures calculated by DFT+U of Hematite cell (a), Fe_2TiO_5 cell (b)
 457 and Hem/ Fe_2TiO_5 construction (c). Corresponding PDOS diagrams of Hematite cell (d), Fe_2TiO_5
 458 cell (e) and Hem/ Fe_2TiO_5 construction (f).

459

460 As one of the prerequisites for the carrier to reach the heterojunction interface and
 461 generate reactive species, the spatial charge density difference (CDD) at the inter-phase
 462 was simulated with varying distances of two phases to further reveal the electron
 463 transfer flows. In concrete terms, the modeled Hematite was utilized as the density
 464 difference set and controlled to be specific distances (3.515 Å, 2.115 Å, 1.216 Å) from
 465 the bottom Fe_2TiO_5 part (Figure S11), then the difference in bonding and electronic
 466 structure between Hematite and Fe_2TiO_5 was computed and visualized in Figure 7a~7c.
 467 Obviously, the electronic structures of the two phases showed basically no effect at a
 468 distance of 3.515 Å, immediately afterward the electrons of Fe on Hematite tended to
 469 transfer to Fe_2TiO_5 contact surface when the distance was reduced to 2.115 Å, and
 470 eventually a more significant electron aggregation on the Fe-O/Ti-O structures of
 471 Fe_2TiO_5 contact interface can be observed when the distance shortened to 1.216 Å.
 472 Additionally, on the basis of the front view of Hem/ Fe_2TiO_5 construction (Figure 7d),

473 2D-CDD mapping and plane-average electron difference plots from sets were extracted
 474 for more accurate evaluation of charge accumulation and depletion. As shown in [Figure](#)
 475 [S12a~12c](#), the electron residue at the Fe_2TiO_5 contact surface and the corresponding
 476 Hematite electron donor region can be seen, indicating the formation of a high-speed
 477 channel for efficient electron transfer [47]. In the plane-average electron difference
 478 plots depicted in [Figure 7e](#), the electron aggregation between two phases and eventual
 479 pooling on the Fe_2TiO_5 contact surface can be found as the distance progressed from
 480 far to near. On the whole, the simulation of Hematite anchoring showed consistent CDD
 481 results with that of XPS and PDOS, the negative charges on Hematite did tend to
 482 migrate to Fe_2TiO_5 on contact. Moreover, the E_f of Hematite and Fe_2TiO_5 rearranged
 483 equilibrium after contact (section 3.4), afterwards a space charge region with strong
 484 internal electric field was formed after the E_f was reached, which could promote the
 485 separation of photogenerated carriers and overall efficiency of degradations [48].

486



487

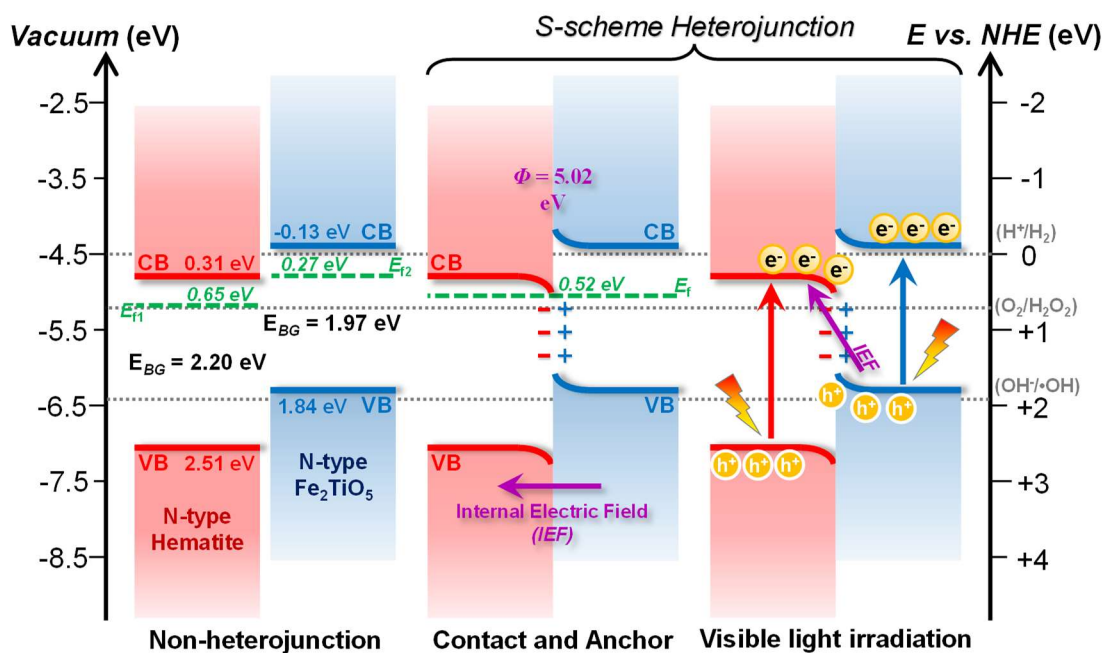
488 **Figure 7** (a~c) Charge density difference (CDD) images at difference spacing distances between
 489 Hematite and Fe_2TiO_5 , where blue and yellow regions indicated the charge accumulation and
 490 depletion, respectively. (d) Front view of as-constructed Hem/ Fe_2TiO_5 for electronic distribution
 491 computation. (e) Plane-average electron difference plots with difference spacing distances of
 492 Hem/ Fe_2TiO_5 .

493

494 *3.6 Heterojunction formation and photocatalytic process proceeding*

495 Based on the previous characterization results and computational inference, the
496 underlying explanation of the S-scheme heterojunction construction process and
497 photocatalytic mechanism of Hem/Fe₂TiO₅ were provided. As shown in [Figure 8](#), both
498 monomers as Hematite and Fe₂TiO₅ exhibited N-type semiconductor properties
499 naturally without heterostructure engineering, whose CB edge surmounted the onset
500 potential for water reduction and thus had possible oxygen reduction capacity [\[49\]](#).
501 However, the band gap of Fe₂TiO₅ (1.97 eV) accompanied by a lower VB (1.84 eV)
502 prevents it from having a significant hole oxidizing capability upon Vis irradiation.
503 Although the VB of Hematite (2.51 eV) seems more favorable, its higher BG (2.20 eV)
504 makes it difficult to be activated by Vis only and generate carriers directly [\[50\]](#). Since
505 Fe₂TiO₅ has a smaller work function with a more negative Fermi energy level, the
506 electrons of anchored Hematite tend to spontaneously diffuse to Fe₂TiO₅ as the two
507 semiconductors have been in contact, forming the electron depletion and accumulation
508 layers and subsequently resulting in the internal electric field (IEF) at the interface of
509 the heterojunction [\[51\]](#). Derive from the formation of S-scheme heterojunction, the
510 overall Fermi energy level is aligned to the same level with simultaneous band bending
511 of the two phases, which in turn reduces the apparent band gap value of Hem/Fe₂TiO₅
512 (1.83 eV). When Vis intervenes to this composite N-N S-scheme heterojunction process,
513 the photogenerated electrons initiate to transfer from CB of Hematite to VB of Fe₂TiO₅
514 due to the presence of IEF, then the recombination of CB electrons and VB holes under
515 coulomb gravity can be referred to the S-type heterojunction process [\[52\]](#). Consequently,
516 as the low reactive photogenerated carriers were eliminated at the heterojunction
517 interface region of Hem/Fe₂TiO₅, the photogenerated holes with higher oxidation
518 potentials are preserved to promote the photocatalytic process.

519



520
521 **Figure 8** Formation procedures of S-scheme N-N heterojunction in Hem/Fe₂TiO₅ and its mechanism
522 of visible light interaction process.

523
524 *3.7 Reactive specie identification and mechanism investigation*

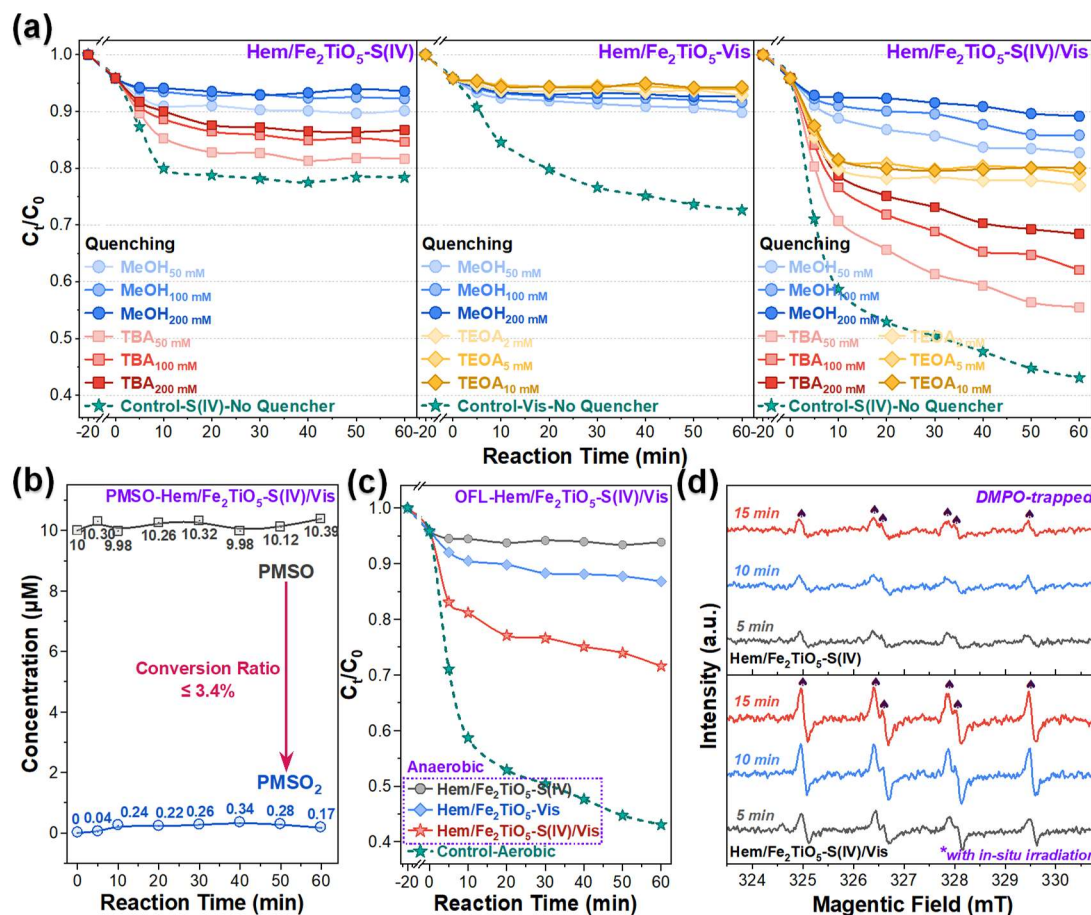
525 For rigorously evaluating the possible reactive species in the coupled Hem/Fe₂TiO₅-
526 S(IV)/Vis system, the presence and contribution of various free radicals were
527 investigated by different quenching experiments (Figure 9a). In the degradation process
528 involving only S(IV), methanol (MeOH, $k(\text{SO}_4^{\cdot-}) = 1.1 \times 10^8 \text{ M}^{-1} \text{ s}^{-1}$, $k(\cdot\text{OH}) = 8.8 \times$
529 $10^8 \text{ M}^{-1} \text{ s}^{-1}$) with different dosages were able to markedly inhibit the vast majority of
530 the degradation process, whereas tert-butanol (TBA, $k(\text{SO}_4^{\cdot-}) = 9.1 \times 10^5 \text{ M}^{-1} \text{ s}^{-1}$, $k(\cdot\text{OH})$
531 $= 7.6 \times 10^8 \text{ M}^{-1} \text{ s}^{-1}$) could only exhibit near half of the quenching effect, suggesting the
532 simultaneous generation of $\text{SO}_4^{\cdot-}$ and $\cdot\text{OH}$ during Hem/Fe₂TiO₅-S(IV) process where
533 the former contributed primarily to the degradation of OFL [25, 53]. As per the
534 difference in photocatalytic performance mediated by Vis, triethanolamine (TEOA) as
535 a sacrificial reagent for photogenerated holes (h^+) showed essentially complete
536 inhibition towards the photocatalytic process [54]. Although MeOH remained a
537 prominent effect on the reaction, the participation of just 2 mM TEOA could terminate
538 the whole photocatalytic reaction, demonstrating the decisive role of h^+ generated by
539 catalyst through the Hem/Fe₂TiO₅-Vis process. Notably in the entire Hem/Fe₂TiO₅-
540 S(IV)/Vis system, the inhibitory effects of MeOH under the same conditions were

541 somewhat weakened but still performed the strongest attenuation for OFL degradation
542 among several quenchers, and the quenching effect by TBA was less pronounced as its
543 concentration decreased, proving the more conclusive contribution of oxy-sulfur
544 radicals [55]. With the addition of TEOA, the subsequent stages of the reaction were
545 significantly inhibited while the reaction initial rate suffered lesser impacts, indicating
546 the essentially unsustainable degradation due to the quenching of h^+ . Additionally, the
547 possible presence of Fe(IV) was also verified by control experiments using methyl
548 phenyl sulfoxide (PMSO) as the substrate (standard curves in Figure S13). As shown
549 in Figure 9b, the conversion rate from PMSO of 10 μ M to methyl phenyl sulfone
550 (PMSO₂) was less than 3.4% in all cases, indicating that there was basically no Fe(IV)
551 involved in the Hem/Fe₂TiO₅-S(IV)/Vis reaction process [56]. Furthermore, oxygen-
552 free control experiments were carried out in several major systems, in which
553 Hem/Fe₂TiO₅-S(IV)/Vis system was able to maintain a more pronounced performance
554 only with irradiation. Attributed to the complete inhibition of anaerobic reaction system
555 with sole S(IV) or apparent decrease with sole Vis, the limitations of indispensable
556 molecular oxygen requirement were certainly addressed with the construction of
557 S(IV)/Vis coupling system (Figure 9c), in other words the photoreactive promotion
558 effect was revealed to be beneficial to the oxy-sulfur radical chain reaction proceedings
559 [11].

560 Afterwards, further identification of the free radicals presented in Hem/Fe₂TiO₅-
561 S(IV)/Vis system was conducted on electron spin resonance (ESR) spectroscopy with
562 in-situ Vis irradiation by applying 2,2,6,6-tetramethyl-4-piperidine (TEMP) and 5,5-
563 Dimethyl-1-pyrroline-N-oxide (DMPO) as the trapping reagents, respectively. As
564 illustrated in Figure S14a, there was no apparent typical signals of TEMPO product can
565 be observed with TEMP trapping, indicating the absence of singlet oxygen (¹O₂) in the
566 composite S(IV)/Vis system whether with Hem/Fe₂TiO₅ or not [57]. For comparison,
567 the radicals formed by the reactions with DMPO exhibited 6-fold considerable
568 hyperfine interaction which could be strengthened over time only with in-situ Vis
569 irradiation (Figure 9d), while similar characteristic signals were not obtained in the
570 S(IV) or S(IV)/Vis processes without Hem/Fe₂TiO₅ involving (Figure S14b). Precisely

571 the strength of the hyperfine interactions is different depending on the trapped radical,
 572 resulting in different spectral shapes depending on the radical properties as well [58].
 573 Hence, the dominant adduct of $\text{DMPO}\cdot\text{SO}_3^-$ can be distinguished by its hyperfine
 574 coupling constants of $\alpha_N = 1.45$ mT and $\alpha_H = 1.61$ mT (Figure S14c) [59], meanwhile
 575 any other significant signals of DMPO adducts were not found in several different
 576 systems, where $\text{SO}_4^{\cdot-}$ and $\cdot\text{OH}$ radicals contributing to the degradations were not
 577 trapped due to the influence of the higher abundance of $\cdot\text{SO}_3^-$ radicals.

578



579

580 **Figure 9** (a) Changes in OFL degradation efficiency of Hem/Fe₂TiO₅-based catalytic systems with
 581 different quenchers with various concentrations. (b) Conversion rate of PMSO₂ under the same
 582 experimental conditions with PMSO as the substrate. (c) Differences in OFL degradation
 583 performance of Hem/Fe₂TiO₅ catalytic systems under aerobic and anoxic conditions. (d) ESR
 584 spectra with DMPO trapping for the Hem/Fe₂TiO₅-S(IV) system with or without in-situ Vis
 585 irradiation.

586

587 As a result, the reaction mechanism of Hem/Fe₂TiO₅-S(IV)/Vis system for OFL
 588 degradation is understood and proposed based on the previous analysis: Firstly, inner-

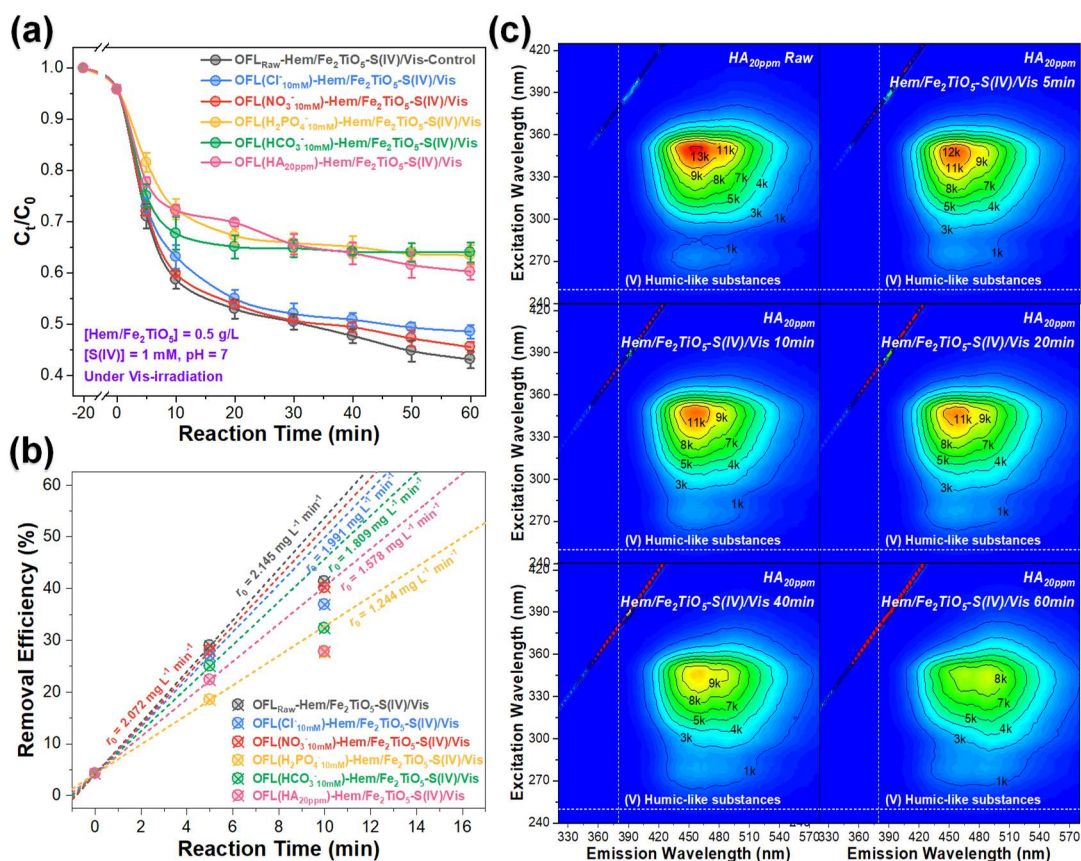
589 sphere complexation ($\equiv\text{Fe(III)}\text{-SO}_3^+$) was formed on site with the surface $\equiv\text{Fe(III)}$ of
590 Hem/ Fe_2TiO_5 with the presence of S(IV), then the sulfite radicals ($\cdot\text{SO}_3^-$) and $\equiv\text{Fe(II)}$
591 were generated simultaneously through the internal electron transfer process of such
592 complexation [25]. Afterwards, vigorous oxidizing species $\text{SO}_4^{\cdot-}$ and $\cdot\text{OH}$ (with
593 intermediate $\text{SO}_5^{\cdot-}$) were further developed through the interaction between $\cdot\text{SO}_3^-$ and
594 molecular oxygen along the oxy-sulfur radical chain reaction [60], which in turn led to
595 the effective degradation of OFL. Meanwhile, Hem/ Fe_2TiO_5 with S-scheme
596 heterojunction properties was activated by visible light (≥ 420 nm) and produced
597 oxidizing h^+ , then being capable of attacking OFL molecules directly or converting
598 S(IV) to $\cdot\text{SO}_3^-$. Thereby, the establishment of h^+ -mediated S(IV)/Vis processes can
599 further promote the overall oxy-sulfur radical chain reaction by accelerating the
600 generation of $\cdot\text{SO}_3^-$ and the proceeding of $\equiv\text{Fe(III)}\text{-}\equiv\text{Fe(II)}\text{-}\equiv\text{Fe(III)}$ regeneration cycle
601 in progress [61], eventually resulting in the more efficient degradation of OFL.
602 Moreover, the $\equiv\text{Fe(II)}$ produced during the reactions was also possible to form $\equiv\text{Fe(II)}\text{-}$
603 SO_3 except being oxidized to $\equiv\text{Fe(III)}$, which could enter the oxy-sulfur radical chain
604 reaction as well through further reaction with h^+ or O_2 . As a result, the participation of
605 h^+ in interfacial reaction promoted the generation of reactive radicals and was also able
606 to substitute for O_2 in DO-involved processes, which has optimized the DO utilization
607 and indeed addressed the limitation of molecular oxygen requirement in the S(IV)-AOP.
608

609 *3.8 Exploration of co-existing substrate effect and system resistance*

610 As the co-existing anions and natural organic matters in aqueous media usually have
611 possible implications on the contaminant treatment efficiency, several typical substrates
612 such as chloride (Cl^-), nitrate (NO_3^-), dihydrogen phosphate (H_2PO_4^-), bicarbonate
613 (HCO_3^-), humic acid (HA) were selected and investigated for their influences on OFL
614 degradation. As displayed in Figures 10a and 10b, the addition of 10 mM NO_3^- had
615 little effect on the performance of Hem/ Fe_2TiO_5 -S(IV)/Vis, while slight inhibition can
616 be observed with 10 mM Cl^- due to its mild quenching effect on both $\text{SO}_4^{\cdot-}$ and $\cdot\text{OH}$
617 radicals [62]. Nevertheless, the presence of both 10 mM HCO_3^- and 10 mM H_2PO_4^-
618 exhibited significant inhibitory effects, wherein the former could equally reduce the

619 overall efficiency through the free radical quenching processes [63]. As regards to
620 H_2PO_4^- , its more affinity with the interface of catalyst could lead to the competitive
621 complexation with desired S(IV), eventually resulting in the occupation of active sites
622 and lower reactivity of the whole system [64]. Additionally, the OFL degradation was
623 also remarkably restrained with 20 ppm HA addition, which could be attributed to the
624 competitive reactions between different substrates and free radicals. As the excitation-
625 emission matrix fluorescence (EEM-FL) spectra shown in Figure 10c, it can be
626 observed that the fluorescence intensity of HA was obviously attenuated by nearly half
627 within 60 min after Hem/ Fe_2TiO_5 -S(IV)/Vis treatment, indicating the decrease in
628 humic-like properties caused by the oxidizing attack [65]. Unfortunately, any obvious
629 fluorescence signals were not obtained in other specific regions, thus it could be
630 hypothesized that valid mineralization and cleavage of HA were difficult to achieve
631 under the conditions set. In addition to the co-existing substrates, the reusability of
632 catalysts is another critical concern in practical water treatment. In this aspect,
633 Hem/ Fe_2TiO_5 catalysts used by different times were collected separately for next run
634 with same conditions. It can be concluded that Hem/ Fe_2TiO_5 could maintain its catalytic
635 capacity after four cycling experiments, though a slight decrease in OFL degradation
636 was observed due to the corrosion effect by S(IV) (Figure S15a). When comparing the
637 XRD patterns of the Hem/ Fe_2TiO_5 used in cycling experiments with the Raw
638 Hem/ Fe_2TiO_5 , it can be seen the essentially identical characteristic signals of them,
639 demonstrating the relatively prominent anti-interference ability and stability of
640 Hem/ Fe_2TiO_5 (Figure S15b).

641



642
 643 **Figure 10** (a) Degradations of OFL in Hem/Fe₂TiO₅-S(IV)/Vis system with different co-existing
 644 substrates. (b) Corresponding initial reaction rates under different influencing factors. (c) Changes
 645 in EEM-FL intensity of degradation processes using HA as the substrate.

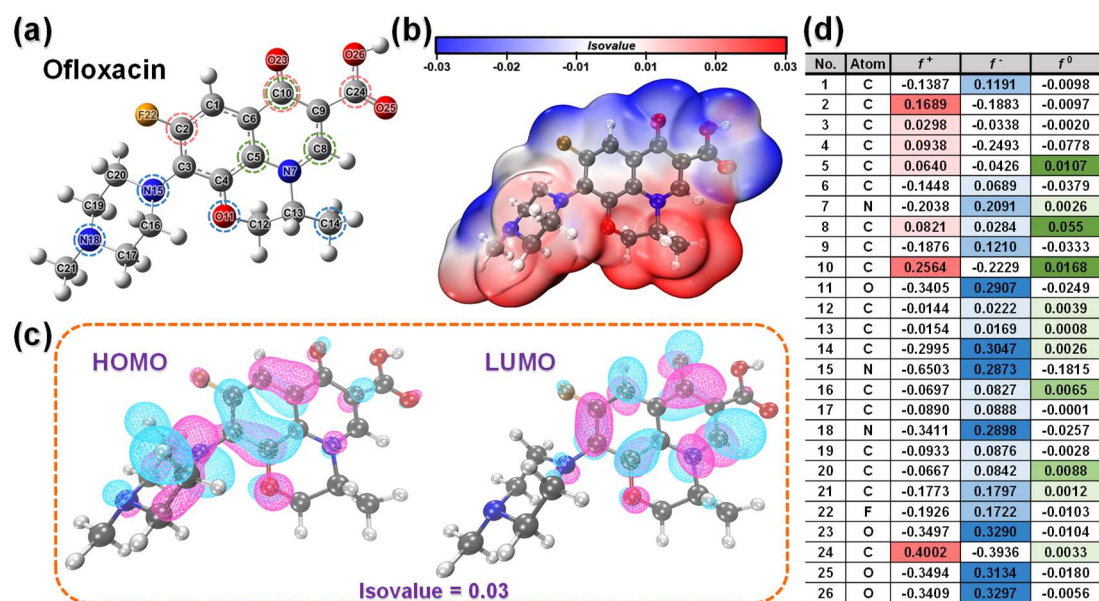
646

647 3.9 Reaction site and degradation pathway interpretation of ofloxacin

648 To investigate the practical process and mechanism of the interaction of the substrate
 649 ofloxacin with reactive radicals in the presented catalyst-S(IV)/Vis system, the
 650 molecular properties of OFL were computed and predicted using density functional
 651 theory (Figure 11a). As confirmed in the previous section, the major contributing
 652 radicals were identified to be SO₄⁻ and [•]OH, which are widely recognized as
 653 electrophilic reagents to attack substrate compounds [66]. Therefore, the identification
 654 and prediction of vulnerable sites on OFL molecule were executed with electrostatic
 655 potential distribution analysis. As illustrated in Figure 11b, N18 as the negative
 656 polarization points on OFL was considered susceptible for electrophilic reactions by
 657 SO₄⁻ and [•]OH radicals, while F22 site was more likely to proceed with electrophilic
 658 substitution reaction for dehalogenation. However, the representative electronic-rich
 659 tendencies involving O23, O25 and O26 were attributed to the influence of O itself,

660 therefore it was not rational to identify them as significant electrophilic sites [67]. In
 661 contrast, C10 and C24 linked to O were denoted as the positive polarization points and
 662 behaved as potential nucleophilic reaction sites. The highest occupied molecular orbital
 663 (HOMO) of OFL indicated the loose binding of electrons near N15, which made it more
 664 likely to lose electrons (Figure 11c). Meanwhile, the lowest unoccupied molecular
 665 orbital (LUMO) exhibited a strong affinity for electrons in the benzene ring and
 666 surrounding heterocycle, indicating the possible nucleophilic reaction sites. Moreover,
 667 the condensed Fukui index for the electrophilic attack was also adopted to quantitatively
 668 describe the potential reactive sites on OFL. As presented in Figures 11a and 11d, the
 669 corresponding Fukui index values were computed and visualized by representative sites,
 670 where O11, C14, N15, N18 showed even higher f^- values and exhibited their potential
 671 for being electrophilic attack, the result was also consistent with the previous analysis
 672 of ESP and HOMO-LUMO.

673



674

675 **Figure 11** (a) Optimized geometry and atomic sequence of the ofloxacin molecule. (b) Electrostatic
 676 potential distribution of OFL molecule. (c) Schematic illustration of HOMO-LUMO molecular
 677 orbitals. (d) Condensed Fukui index from natural population analysis charges of OFL.

678

679 To validate the theoretical computation results and further ascertain the degradation
 680 pathway of OFL, the primary intermediates of OFL-Hem/Fe₂TiO₅-S(IV)/Vis process
 681 were identified by liquid chromatography-mass spectrometry (LC-MS). The mass

682 spectra and corresponding possible chemical structures were provided in [Figure S16](#)
683 and [Table S4](#), respectively. Based on the detected mass/charge (m/z) values and related
684 literatures, the possible degradation pathways were deduced in [Figure 12](#). Generally,
685 Int 1 and Int 2 can be produced by direct sulfonation and hydroxylation of OFL
686 molecule, respectively, where Int 2 can also be obtained by the electrophilic substitution
687 process of Int 1, thus further degradation initiated with mainly the hydroxylated OFL
688 (Int 2). Similar to the previous theoretical computation results, the piperazine ring
689 exhibited higher frontier electron density and oxidability, thus the cleavage of the OFL
690 molecule was primarily initiated by the piperazine ring [\[68\]](#). Consequently, Int 3 and
691 Int 10 were derived from the oxidative decomposition and dehydration of Int 2, then Int
692 3 was further converted to Int 4 and Int 5 with gradual removal of N from the piperazine
693 ring and completion of demethylation. Afterwards, Int 6 and Int 7 were generated from
694 the promoter Int 5 via decarboxylation reaction and re-demethylation, and F site in the
695 molecule underwent electrophilic substitution to form Int 8 with defluorination
696 completed [\[69\]](#). Thereafter, the cleavage of oxazine ring resulted in the formation of Int
697 9, which could continue to be further oxidized to fatty acids and smaller product
698 molecules. In addition to the above intermediate decomposed products, various
699 compounds in different pathways such as Int 11 and Int 15 can be detected due to the
700 diversified cleavage of piperazine ring, and successive degradation by corresponding
701 processes was basically dominated by the decarboxylation on the double bond C and
702 demethylation of the oxazine ring (Int 12, Int 13, Int 14, Int 16), which was followed
703 by dehalogenation and further oxidation to the subsequent products [\[70\]](#). Alternatively,
704 OFL can be reacted directly by carbonylation to produce Int 17, then proceed with
705 similar oxidative decomposition processes to smaller molecules such as Int 18, Int 19,
706 etc. Hence, it was found that the majority of the compounds generated during the
707 Hem/Fe₂TiO₅-S(IV)/Vis degradation preserved the main structure of OFL, with the
708 principal decomposition occurring in the N piperazine ring.
709

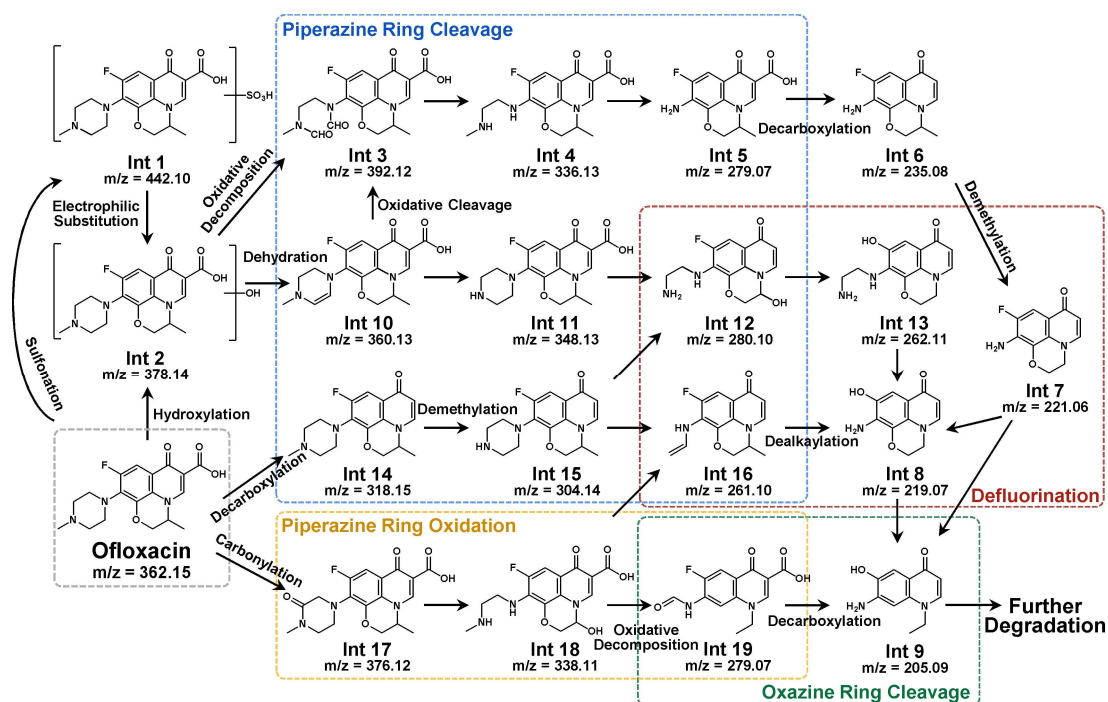


Figure 12 Possible degradation pathways of ofloxacin by Hem/Fe₂TiO₅ system.

710

711

712

713 4. Conclusions

714 In this work, an S-scheme heterojunction catalyst defined as Hem/Fe₂TiO₅ was
 715 constructed by in-situ Hematite anchoring on the Fe₂TiO₅ interface, which was more
 716 reactive with S(IV) and exhibited enhanced visible light responsiveness, and was
 717 further utilized for the establishment of S(IV)/Vis coupled system to possess ofloxacin
 718 degradation under neutral conditions. Notably, at a higher OFL concentration of 50 ppm
 719 (138.4 μM) and initial S(IV) of 1 mM, Hem/Fe₂TiO₅ dosed at 0.5 g/L was capable of
 720 achieving more than 50% substrate removal in 60 min under Vis irradiation (≥ 420 nm,
 721 115.3 mW/cm²), with a superior initial rate of $r_0 = 2.145 \text{ mg L}^{-1} \text{ min}^{-1}$ nearly four times
 722 as much compared to Fe₂TiO₅. As the in-depth investigation of the degradation
 723 performance differences under various conditions (pH, DO, initial dosages and
 724 concentrations) proceeded, the role and critical contribution of Vis in S(IV)-AOPs were
 725 probed and confirmed, which in turn elucidates the potential advantages of the as-
 726 applied Hem/Fe₂TiO₅-S(IV)/Vis process for conducting the activation of oxy-sulfur
 727 radical chain reactions and photogenerated carriers simultaneously. Additionally, the
 728 formation of an internal electric field on the heterogenous interface between anchored

729 Hematite and Fe_2TiO_5 was verified by characterizations and theoretical computations,
730 which can effectively enhance the separation efficiency and reduce the resistance for
731 realizing the carrier modulation and energy band structure optimization. Eventually, the
732 principal active species during the degradation process were identified as $\text{SO}_4^{\bullet-}$ and
733 $\cdot\text{OH}$ radicals, while the mechanism of Vis promotion towards the oxy-sulfur radical
734 chain reactions in S(IV)-AOP was also revealed. Besides, the specific degradation
735 pathways were proposed through products identification with mass spectrometry in
736 combination with calculation of potential reactive sites on OFL molecular.

737 **Credit authorship contribution statement**

738 **Wenyu Wang:** Conceptualization, Data curation, Formal analysis, Investigation,
739 Visualization, Writing-Original draft. **Juntao Guo:** Methodology, Investigation, Data
740 curation. **Yihui Zhang:** Methodology, Formal analysis. **Kun Lu:** Formal analysis. **Jing**
741 **Xu:** Validation, Formal analysis. **Jinjun Li:** Writing-Review & Editing. **Gilles Mailhot:**
742 Conceptualization, Writing-Review & Editing. **Feng Wu:** Conceptualization, Project
743 administration, Writing-Review & Editing, Funding acquisition, Supervision.

744

745 **Acknowledgments**

746 The authors gratefully acknowledge the financially supports by the National Natural
747 Science Foundation of China (No. 22376167 and 22061132001), and the project I-Site
748 CAP 20-25 through the LIA «Laboratory of Environmental Processes Remediation».
749 The authors appreciate helpful comments from the editors and reviewers.

750 **References**

- 751 [1] V.T. Andriole, The Quinolones: Past, Present, and Future, *Clin. Infect. Dis.*, 41 (2005) S113-
752 S119. <https://doi.org/10.1086/428051>.
- 753 [2] L.W. Matzek, K.E. Carter, Activated persulfate for organic chemical degradation: A review,
754 *Chemosphere*, 151 (2016) 178-188. <https://doi.org/10.1016/j.chemosphere.2016.02.055>.
- 755 [3] G. Fang, J. Gao, D.D. Dionysiou, C. Liu, D. Zhou, Activation of persulfate by quinones: free
756 radical reactions and implication for the degradation of PCBs, *Environ. Sci. Technol.*, 47 (2013)
757 4605-4611. <https://doi.org/10.1021/es400262n>.
- 758 [4] K.S. Sra, N.R. Thomson, J.F. Barker, Persistence of Persulfate in Uncontaminated Aquifer
759 Materials, *Environ. Sci. Technol.*, 44 (2010) 3098-3104. <https://doi.org/10.1021/es903480k>.
- 760 [5] Z. Liu, S. Yang, Y. Yuan, J. Xu, Y. Zhu, J. Li, F. Wu, A novel heterogeneous system for sulfate
761 radical generation through sulfite activation on a CoFe_2O_4 nanocatalyst surface, *J. Hazard. Mater.*,
762 324 (2017) 583-592. <https://doi.org/10.1016/j.jhazmat.2016.11.029>.
- 763 [6] D. Zhou, L. Chen, J. Li, F. Wu, Transition metal catalyzed sulfite auto-oxidation systems for
764 oxidative decontamination in waters: A state-of-the-art minireview, *Chem. Eng. J.*, 346 (2018) 726-
765 738. <https://doi.org/10.1016/j.cej.2018.04.016>.
- 766 [7] M.H. Conklin, M.R. Hoffmann, Metal ion-sulfur(IV) chemistry. 2. Kinetic studies of the redox
767 chemistry of copper(II)-sulfur(IV) complexes, *Environ. Sci. Technol.*, 22 (1988) 891-898.
768 <https://doi.org/10.1021/es00173a005>.
- 769 [8] D.T.F. Kuo, D.W. Kirk, C.Q. Jia, The chemistry of aqueous S(IV)-Fe-O₂ system: state of the art,
770 *J. Sulfur Chem.*, 27 (2007) 461-530. <https://doi.org/10.1080/17415990600945153>.
- 771 [9] S.-R. Zhu, J.-N. Yang, Y. Liu, W. Gao, X. Yi, H. Zhou, M. Wu, Synergetic interaction of lithium
772 cobalt oxide with sulfite to accelerate the degradation of organic aqueous pollutants, *Mater. Chem.*
773 *Phys.*, 249 (2020) 123123. <https://doi.org/10.1016/j.matchemphys.2020.123123>.
- 774 [10] Z. Jia, J. Kang, W.C. Zhang, W.M. Wang, C. Yang, H. Sun, D. Habibi, L.C. Zhang, Surface
775 aging behaviour of Fe-based amorphous alloys as catalysts during heterogeneous photo Fenton-like
776 process for water treatment, *Appl. Catal. B Environ.*, 204 (2017) 537-547.
777 <https://doi.org/10.1016/j.apcatb.2016.12.001>.
- 778 [11] A. Abdelhaleem, W. Chu, X. Liang, Diphenamid degradation via sulfite activation under visible
779 LED using Fe (III) impregnated N-doped TiO₂ photocatalyst, *Appl. Catal. B Environ.*, 244 (2019)
780 823-835. <https://doi.org/10.1016/j.apcatb.2018.11.085>.
- 781 [12] J. Ma, L. Chen, Y. Liu, T. Xu, H. Ji, J. Duan, F. Sun, W. Liu, Oxygen defective titanate
782 nanotubes induced by iron deposition for enhanced peroxymonosulfate activation and
783 acetaminophen degradation: Mechanisms, water chemistry effects, and theoretical calculation, *J.*
784 *Hazard. Mater.*, 418 (2021) 126180. <https://doi.org/10.1016/j.jhazmat.2021.126180>.
- 785 [13] O. Linnik, N. Chorna, N. Smirnova, Non-porous Iron Titanate Thin Films Doped with Nitrogen:
786 Optical, Structural, and Photocatalytic Properties, *Nanoscale Res. Lett.*, 12 (2017) 249.
787 <https://doi.org/10.1186/s11671-017-2027-7>.
- 788 [14] C.C. Li, A. Li, Z.B. Luo, J.J. Zhang, X.X. Chang, Z.Q. Huang, T. Wang, J.L. Gong, Surviving
789 High-Temperature Calcination: ZrO₂-Induced Hematite Nanotubes for Photoelectrochemical Water
790 Oxidation, *Angew. Chem. Int. Edit.*, 56 (2017) 4150-4155. <https://doi.org/10.1002/anie.201611330>.

791 [15] L. Wang, N.T. Nguyen, X. Huang, P. Schmuki, Y. Bi, Hematite Photoanodes: Synergetic
792 Enhancement of Light Harvesting and Charge Management by Sandwiched with Fe₂TiO₅/Fe₂O₃/Pt
793 Structures, *Adv. Funct. Mater.*, 27 (2017) 1703527. <https://doi.org/10.1002/adfm.201703527>.

794 [16] F. Wang, H.C. Yu, M.H. Chen, L. Wu, N. Pereira, K. Thornton, A. Van der Ven, Y. Zhu, G.G.
795 Amatucci, J. Graetz, Tracking lithium transport and electrochemical reactions in nanoparticles, *Nat.*
796 *Commun.*, 3 (2012) 1201. <https://doi.org/10.1038/ncomms2185>.

797 [17] N.A. Seaton, Determination of the connectivity of porous solids from nitrogen sorption
798 measurements, *Chem. Eng. Sci.*, 46 (1991) 1895-1909. [https://doi.org/10.1016/0009-
799 2509\(91\)80151-N](https://doi.org/10.1016/0009-2509(91)80151-N).

800 [18] Z. Zhang, R. Ji, Q. Sun, J. He, D. Chen, N. Li, H. Li, A. Marcomini, Q. Xu, J. Lu, Enhanced
801 photocatalytic degradation of 2-chlorophenol over Z-scheme heterojunction of CdS-decorated
802 oxygen-doped g-C₃N₄ under visible-light, *Appl. Catal. B Environ.*, 324 (2023) 122276.
803 <https://doi.org/10.1016/j.apcatb.2022.122276>.

804 [19] B. Sharma, P.K. Boruah, A. Yadav, M.R. Das, TiO₂-Fe₂O₃ nanocomposite heterojunction for
805 superior charge separation and the photocatalytic inactivation of pathogenic bacteria in water under
806 direct sunlight irradiation, *J. Environ. Chem. Eng.*, 6 (2018) 134-145.
807 <https://doi.org/10.1016/j.jece.2017.11.025>.

808 [20] H. Li, Q. Zhou, F. Liu, W. Zhang, Z. Tan, H. Zhou, Z. Huang, S. Jiao, Y. Kuang, Biomimetic
809 design of ultrathin edge-riched FeOOH@Carbon nanotubes as high-efficiency electrocatalysts for
810 water splitting, *Appl. Catal. B Environ.*, 255 (2019) 117755.
811 <https://doi.org/10.1016/j.apcatb.2019.117755>.

812 [21] B. Bharti, S. Kumar, H.N. Lee, R. Kumar, Formation of oxygen vacancies and Ti³⁺ state in TiO₂
813 thin film and enhanced optical properties by air plasma treatment, *Sci. Rep.*, 6 (2016) 32355.
814 <https://doi.org/10.1038/srep32355>.

815 [22] C.C. Li, T. Wang, Z.B. Luo, S.S. Liu, J.L. Gong, Enhanced Charge Separation through ALD-
816 Modified Fe₂O₃/Fe₂TiO₅ Nanorod Heterojunction for Photoelectrochemical Water Oxidation, *Small*,
817 12 (2016) 3415-+. <https://doi.org/10.1002/smll.201600940>.

818 [23] J. Fu, Q. Xu, J. Low, C. Jiang, J. Yu, Ultrathin 2D/2D WO₃/g-C₃N₄ step-scheme H₂-production
819 photocatalyst, *Appl. Catal. B Environ.*, 243 (2019) 556-565.
820 <https://doi.org/10.1016/j.apcatb.2018.11.011>.

821 [24] X.Y. Wang, Y.S. Wang, M.C. Gao, J.N. Shen, X.P. Pu, Z.Z. Zhang, H.X. Lin, X.X. Wang,
822 BiVO₄/Bi₄Ti₃O₁₂ heterojunction enabling efficient photocatalytic reduction of CO₂ with H₂O to
823 CH₃OH and CO, *Appl. Catal. B Environ.*, 270 (2020) 9.
824 <https://doi.org/10.1016/j.apcatb.2020.118876>.

825 [25] W. Ding, W. Xiao, W. Huang, Q. Sun, H. Zheng, Sulfite activation on a silica-supported well-
826 dispersed cobalt catalyst via an electron transfer complex path, *J. Cleaner Prod.*, 257 (2020) 120457.
827 <https://doi.org/10.1016/j.jclepro.2020.120457>.

828 [26] Y. Zhang, W. Chu, Enhanced degradation of metronidazole by cobalt doped TiO₂/sulfite process
829 under visible light, *Sep. Purif. Technol.*, 291 (2022) 120900.
830 <https://doi.org/10.1016/j.seppur.2022.120900>.

831 [27] J. Berglund, S. Fronaeus, L.I. Elding, Kinetics and mechanism for manganese-catalyzed
832 oxidation of sulfur (IV) by oxygen in aqueous solution, *Inorg. Chem.*, 32 (1993) 4527-4538.
833 <https://doi.org/10.1021/ic00073a011>.

- 834 [28] J. Qiao, L. Feng, H. Dong, Z. Zhao, X. Guan, Overlooked Role of Sulfur-Centered Radicals
835 During Bromate Reduction by Sulfite, *Environ. Sci. Technol.*, 53 (2019) 10320-10328.
836 <https://doi.org/10.1021/acs.est.9b01783>.
- 837 [29] B.K. Heragh, S. Javanshir, G.R. Mahdavinia, M.R.N. Jamal, Hydroxyapatite grafted
838 chitosan/laponite RD hydrogel: Evaluation of the encapsulation capacity, pH-responsivity, and
839 controlled release behavior, *Int. J. Biol. Macromol.*, 190 (2021) 351-359.
840 <https://doi.org/10.1016/j.ijbiomac.2021.08.220>.
- 841 [30] W. Yang, G. Dang, M. Fujii, C. Cai, Y. Wei, Y. Zhang, Heterogeneous Activation of Sulfite by
842 a Three-Dimensional Printed Hierarchically Porous Copper Catalyst for the Degradation of
843 Tetracycline Hydrochloride in Water, *ACS ES&T Water*, 4 (2024) 1730–1740.
844 <https://doi.org/10.1021/acsestwater.3c00771>.
- 845 [31] R.B.P. Marcelino, C.C. Amorim, Towards visible-light photocatalysis for environmental
846 applications: band-gap engineering versus photons absorption-a review, *Environ. Sci. Pollut. Res.*,
847 26 (2019) 4155-4170. <https://doi.org/10.1007/s11356-018-3117-5>.
- 848 [32] N.G. Menon, S.S.V. Tatiparti, S. Mukherji, Synthesis, characterization and photocatalytic
849 activity evaluation of TiO₂-ZnO nanocomposites: Elucidating effect of varying Ti:Zn molar ratio,
850 *Colloids and Surfaces A: Physicochemical and Engineering Aspects*, 565 (2019) 47-58.
851 <https://doi.org/10.1016/j.colsurfa.2018.12.053>.
- 852 [33] L. Chen, X. Peng, J. Liu, J. Li, F. Wu, Decolorization of Orange II in Aqueous Solution by an
853 Fe(II)/sulfite System: Replacement of Persulfate, *Ind. Eng. Chem. Res.*, 51 (2012) 13632-13638.
854 <https://doi.org/10.1021/ie3020389>.
- 855 [34] U. Lamdab, K. Wetchakun, S. Phanichphant, W. Kangwansupamonkon, N. Wetchakun, Highly
856 efficient visible light-induced photocatalytic degradation of methylene blue over InVO₄/BiVO₄
857 composite photocatalyst, *J. Mater. Sci.*, 50 (2015) 5788-5798. <https://doi.org/10.1007/s10853-015-9126-6>.
- 859 [35] Z. Chen, H. Yin, R. Wang, Y. Peng, C. You, J. Li, Efficient Electron Transfer by Plasmonic
860 Silver in SrTiO₃ for Low-Concentration Photocatalytic NO Oxidation, *Environ. Sci. Technol.*, 56
861 (2022) 3604-3612. <https://doi.org/10.1021/acs.est.2c00262>.
- 862 [36] V.M. Nikolic, S.L. Maslovara, G.S. Tasic, T.P. Brdaric, P.Z. Lausevic, B.B. Radak, M.P.
863 Marceta Kaninski, Kinetics of hydrogen evolution reaction in alkaline electrolysis on a Ni cathode
864 in the presence of Ni–Co–Mo based ionic activators, *Appl. Catal. B Environ.*, 179 (2015) 88-94.
865 <https://doi.org/10.1016/j.apcatb.2015.05.012>.
- 866 [37] X. Zhu, Z. Cao, W. Wang, H. Li, J. Dong, S. Gao, D. Xu, L. Li, J. Shen, M. Ye, Superior-
867 Performance Aqueous Zinc-Ion Batteries Based on the In Situ Growth of MnO₂ Nanosheets on
868 V₂CT_x MXene, *ACS Nano*, 15 (2021) 2971-2983. <https://doi.org/10.1021/acsnano.0c09205>.
- 869 [38] P.S. Bassi, R.P. Antony, P.P. Boix, Y. Fang, J. Barber, L.H. Wong, Crystalline Fe₂O₃/Fe₂TiO₅
870 heterojunction nanorods with efficient charge separation and hole injection as photoanode for solar
871 water oxidation, *Nano Energy*, 22 (2016) 310-318. <https://doi.org/10.1016/j.nanoen.2016.02.013>.
- 872 [39] S. Majumder, X. Su, K.H. Kim, Effective strategy of incorporating Co₃O₄ as a co-catalyst onto
873 an innovative BiVO₄/Fe₂TiO₅ core-shell heterojunction for effective photoelectrochemical water-
874 splitting application, *Surf. Interfaces*, 39 (2023) 102936.
875 <https://doi.org/10.1016/j.surfin.2023.102936>.
- 876 [40] Y. Hou, X. Du, S. Scheiner, D.P. McMeekin, Z. Wang, N. Li, M.S. Killian, H. Chen, M. Richter,

877 I. Levchuk, N. Schrenker, E. Spiecker, T. Stubhan, N.A. Luechinger, A. Hirsch, P. Schmuki, H.P.
878 Steinruck, R.H. Fink, M. Halik, H.J. Snaith, C.J. Brabec, A generic interface to reduce the efficiency-
879 stability-cost gap of perovskite solar cells, *Science*, 358 (2017) 1192-1197.
880 <https://doi.org/10.1126/science.aao5561>.

881 [41] Y. Wang, J. Li, Y. Zhou, Z. Gao, W. Zhu, L. Liu, Interfacial defect mediated charge carrier
882 trapping and recombination dynamics in TiO₂-based nanoheterojunctions, *J. Alloys Compd.*, 872
883 (2021) 159592. <https://doi.org/10.1016/j.jallcom.2021.159592>.

884 [42] D.H. Seo, S.Y. Hong, T.H. You, A. Sivanantham, I.S. Cho, Using a CeO₂ quantum dot hole
885 extraction-layer for enhanced solar water splitting activity of BiVO₄ photoanodes, *Chem. Eng. J.*,
886 450 (2022) 137917. <https://doi.org/10.1016/j.cej.2022.137917>.

887 [43] B.G. Janesko, Replacing hybrid density functional theory: motivation and recent advances,
888 *Chem. Soc. Rev.*, 50 (2021) 8470-8495. <https://doi.org/10.1039/d0cs01074j>.

889 [44] N. Naveas, R. Pulido, C. Marini, J. Hernandez-Montelongo, M.M. Silvan, First-principles
890 calculations of hematite (alpha-Fe₂O₃) by self-consistent DFT+U+V, *iScience*, 26 (2023) 106033.
891 <https://doi.org/10.1016/j.isci.2023.106033>.

892 [45] L. Jin, C. Zhou, Electronic structures and optic properties of Fe₂TiO₅ using LSDA+U approach,
893 *Prog. Nat. Sci-Mater.*, 23 (2013) 413-419. <https://doi.org/10.1016/j.pnsc.2013.06.012>.

894 [46] Q. Wang, D. Xu, Y. Dong, S. Pang, L. Zhang, G. Zhang, L. Lv, X. Liu, Y. Xia, L.C. Campos,
895 Z. Ren, P. Wang, Unsaturated Nd-Bi dual-metal sites enable efficient NIR light-driven O₂ activation
896 for water purification, *Appl. Catal. B Environ.*, 319 (2022).
897 <https://doi.org/10.1016/j.apcatb.2022.121924>.

898 [47] F. Zhang, X. Li, Q. Zhao, G. Chen, Q. Zhang, High-performance In₂O₃@PANI core@shell
899 architectures with ultralong charge carriers lifetime for photocatalytic degradation of gaseous 1,2-
900 dichlorobenzene, *Appl. Catal. B Environ.*, 263 (2020) 118278.
901 <https://doi.org/10.1016/j.apcatb.2019.118278>.

902 [48] A. Wang, W. Wang, J. Ni, D. Liu, D. Liu, J. Ma, X. Jia, MOF derived ZnO clusters on ultrathin
903 Bi₂MoO₆ yolk@shell reactor: Establishing carrier transfer channel via PANI tandem S-scheme
904 heterojunction, *Appl. Catal. B Environ.*, 328 (2023) 122492.
905 <https://doi.org/10.1016/j.apcatb.2023.122492>.

906 [49] P.S. Bassi, S.Y. Chiam, Gurudayal, J. Barber, L.H. Wong, Hydrothermal grown nanoporous
907 iron based titanate, Fe₂TiO₅ for light driven water splitting, *ACS Appl. Mater. Interfaces*, 6 (2014)
908 22490-22495. <https://doi.org/10.1021/am5065574>.

909 [50] K. Sivula, F. Le Formal, M. Gratzel, Solar Water Splitting: Progress Using Hematite (alpha-
910 Fe₂O₃) Photoelectrodes, *ChemSusChem*, 4 (2011) 432-449. <https://doi.org/10.1002/cssc.201000416>.

911 [51] J. Mu, F. Teng, H. Miao, Y. Wang, X. Hu, In-situ oxidation fabrication of 0D/2D SnO₂/SnS₂
912 novel Step-scheme heterojunctions with enhanced photoelectrochemical activity for water splitting,
913 *Appl. Surf. Sci.*, 501 (2020) 143974. <https://doi.org/10.1016/j.apsusc.2019.143974>.

914 [52] Q. Xu, L. Zhang, B. Cheng, J. Fan, J. Yu, S-Scheme Heterojunction Photocatalyst, *Chem.*, 6
915 (2020) 1543-1559. <https://doi.org/10.1016/j.chempr.2020.06.010>.

916 [53] W. Xian, W. Wang, J. Guo, J. Li, J. Xu, F. Wu, FePO₄ activated sulfite autoxidation for
917 simultaneous pollutant degradation and phosphorus release, *J. Cleaner Prod.*, 445 (2024) 141342.
918 <https://doi.org/10.1016/j.jclepro.2024.141342>.

919 [54] Y. Li, Z. Ruan, Y. He, J. Li, K. Li, Y. Jiang, X. Xu, Y. Yuan, K. Lin, In situ fabrication of
920 hierarchically porous g-C₃N₄ and understanding on its enhanced photocatalytic activity based on
921 energy absorption, *Appl. Catal. B Environ.*, 236 (2018) 64-75.
922 <https://doi.org/10.1016/j.apcatb.2018.04.082>.

923 [55] W. Peng, Y. Lin, Z. Wan, H. Ji, W. Ma, J. Zhao, An unusual dependency on the hole-scavengers
924 in photocatalytic reductions mediated by a titanium-based metal-organic framework, *Catal. Today*,
925 340 (2020) 86-91. <https://doi.org/10.1016/j.cattod.2018.11.038>.

926 [56] H. Dong, Y. Li, S. Wang, W. Liu, G. Zhou, Y. Xie, X. Guan, Both Fe(IV) and Radicals Are
927 Active Oxidants in the Fe(II)/Peroxydisulfate Process, *Environ. Sci. Technol. Lett.*, 7 (2020) 219-
928 224. <https://doi.org/10.1021/acs.estlett.0c00025>.

929 [57] Z.Y. Ma, P.H. Li, L.Q. Ye, Y. Zhou, F.Y. Su, C.H. Ding, H.Q. Xie, Y. Bai, P.K. Wong, Oxygen
930 vacancies induced exciton dissociation of flexible BiOCl nanosheets for effective photocatalytic
931 CO₂ conversion, *J. Mater. Chem. A*, 5 (2017) 24995-25004. <https://doi.org/10.1039/c7ta08766g>.

932 [58] S.A. Bonke, T. Risse, A. Schnegg, A. Brückner, In situ electron paramagnetic resonance
933 spectroscopy for catalysis, *Nature Reviews Methods Primers*, 1 (2021) 295-310.
934 <https://doi.org/10.1038/s43586-021-00031-4>.

935 [59] C. Mottley, R.P. Mason, Sulfate Anion Free Radical Formation by the Peroxidation of
936 (Bi)sulfite and Its Reaction with Hydroxyl Radical Scavengers, *Arch. Biochem. Biophys.*, 267 (1988)
937 681-689. [https://doi.org/10.1016/0003-9861\(88\)90077-X](https://doi.org/10.1016/0003-9861(88)90077-X).

938 [60] Y.Q. Chen, M.Y. Li, Y. Tong, Z.Z. Liu, L.P. Fang, Y. Wu, Z. Fang, F. Wu, L.Z. Huang, Radical
939 generation via sulfite activation on NiFe₂O₄ surface for estriol removal: Performance and
940 mechanistic studies, *Chem. Eng. J.*, 368 (2019) 495-503. <https://doi.org/10.1016/j.cej.2019.02.196>.

941 [61] D. Zhou, L. Chen, C. Zhang, Y. Yu, L. Zhang, F. Wu, A novel photochemical system of ferrous
942 sulfite complex: kinetics and mechanisms of rapid decolorization of Acid Orange 7 in aqueous
943 solutions, *Water Res.*, 57 (2014) 87-95. <https://doi.org/10.1016/j.watres.2014.03.016>.

944 [62] G.V. Buxton, C.L. Greenstock, W.P. Helman, A.B. Ross, Critical Review of Rate Constants for
945 Reactions of Hydrated Electrons, Hydrogen Atoms and Hydroxyl Radicals ($\cdot\text{OH}/\cdot\text{O}$ -) in Aqueous
946 Solution, *J. Phys. Chem. Ref. Data*, 17 (1988) 513-886. <https://doi.org/10.1063/1.555805>.

947 [63] X. Ao, W. Liu, Degradation of sulfamethoxazole by medium pressure UV and oxidants:
948 Peroxymonosulfate, persulfate, and hydrogen peroxide, *Chem. Eng. J.*, 313 (2017) 629-637.
949 <https://doi.org/10.1016/j.cej.2016.12.089>.

950 [64] Y. Ren, L. Lin, J. Ma, J. Yang, J. Feng, Z. Fan, Sulfate radicals induced from peroxydisulfate
951 by magnetic ferrosin MF₂O₄ (M = Co, Cu, Mn, and Zn) as heterogeneous catalysts in the water,
952 *Appl. Catal. B Environ.*, 165 (2015) 572-578. <https://doi.org/10.1016/j.apcatb.2014.10.051>.

953 [65] P. Xie, L. Zhang, J. Chen, J. Ding, Y. Wan, S. Wang, Z. Wang, A. Zhou, J. Ma, Enhanced
954 degradation of organic contaminants by zero-valent iron/sulfite process under simulated sunlight
955 irradiation, *Water Res.*, 149 (2019) 169-178. <https://doi.org/10.1016/j.watres.2018.10.078>.

956 [66] C. Jiang, Y. Ji, Y. Shi, J. Chen, T. Cai, Sulfate radical-based oxidation of fluoroquinolone
957 antibiotics: Kinetics, mechanisms and effects of natural water matrices, *Water Res.*, 106 (2016) 507-
958 517. <https://doi.org/10.1016/j.watres.2016.10.025>.

959 [67] J. Cao, Q. Ren, F. Chen, T. Lu, Comparative study on the methods for predicting the reactive
960 site of nucleophilic reaction, *Sci. China Chem.*, 58 (2015) 1845-1852.
961 <https://doi.org/10.1007/s11426-015-5494-7>.

- 962 [68] Q. Wang, B. Wang, Y. Ma, S. Xing, Enhanced superoxide radical production for ofloxacin
963 removal via persulfate activation with Cu-Fe oxide, *Chem. Eng. J.*, 354 (2018) 473-480.
964 <https://doi.org/10.1016/j.cej.2018.08.055>.
- 965 [69] R. Patidar, V.C. Srivastava, Mechanistic insight into ultrasound-induced enhancement of
966 electrochemical oxidation of ofloxacin: Multi-response optimization and cost analysis,
967 *Chemosphere*, 257 (2020) 127121. <https://doi.org/10.1016/j.chemosphere.2020.127121>.
- 968 [70] Z. Zhang, X. Xie, Z. Yu, H. Cheng, Influence of chemical speciation on photochemical
969 transformation of three fluoroquinolones (FQs) in water: Kinetics, mechanism, and toxicity of
970 photolysis products, *Water Res.*, 148 (2019) 19-29. <https://doi.org/10.1016/j.watres.2018.10.027>.
- 971